IMPLEMENTATION OF INTERNAL WAVE APPARATUS FOR COPEPOD BEHAVIOR ASSAYS

A Thesis
Presented to
The Academic Faculty

by

Seongyu Jung

In Partial Fulfillment
of the Requirements for the Degree
Master of Science in the
School of Civil and Environmental Engineering

Georgia Institute of Technology
December 2015

Copyright © 2015 by Seongyu Jung

IMPLEMENTATION OF INTERNAL WAVE APPARATUS FOR COPEPOD BEHAVIOR ASSAYS

Approved by:

Dr. Donald R. Webster, Advisor
School of Civil and Environmental Engineering
Georgia Institute of Technology

Dr. Kevin A. Haas
School of Civil and Environmental Engineering
Georgia Institute of Technology

Dr. Jeannette Yen
School of Biology
Georgia Institute of Technology

Date Approved: 3 December 2015

ACKNOWLEDGEMENTS

I am tremendously grateful for number of people who allowed me to go through the process of writing this thesis. First, I would like to thank and return all glory to Jesus Christ, my personal Lord and Savior. The sense of true peace and thankfulness in all I do through the filling of the Holy Spirit really gave me strength to finish. My loving parents, without your unending love, care, and attention to me I would not have been able to do anything. Thank you for showing me what true love is. Michelle, thank you for allowing me to vent and complain to release my stress, and for supporting me through my ups and downs.

Dr. Webster, there is no way I could have completed my graduate work without your expertise and patience. Your dedication to your students, both undergrad and graduate alike, is far greater than that of any other professors I have seen on campus. I truly admire the time and effort you put into us. Thank you for your knowledge and time that you have invested in me. Dr. Haas, I want to apologize and thank you for all the times I bothered you with mountains of questions. I am forever grateful for your willingness to answer all of my questions regardless of how repetitive they may have been. I truly appreciated your open door policy. Dr. Yen, I admire your enthusiasm for your research and want to thank you for your advice. I hope to have a passion for my future work as you do for your research.

I want to also express my gratitude to a single individual who basically carried me through the design and fabrication of my internal wave apparatus. Mr. Andy Udell, thank you for your time and knowledge in everything you do. I appreciate your patience in showing me the basics of all the lab equipments and helping me in resolving all the issues I had in the lab. I probably would have flooded the whole cold

room as well as break all the lab equipment if it was not for your help and guidance.

Lastly, I want to thank my awesome labmates for making my times in the windowless office bearable: Aaron True (thank you for all the fun times during Track-a-thon and always readily answering my questions all the way from CO!), Deepak Adhikari (for teaching me how to have fun at conferences and introducing me to many great people from MN), David Young (for all the Smokeapaloozas and the treats you bring us - I probably gained about 20 lbs. but that's okay!), and Anna Skipper (for being both a great work friend and a classmate - I probably would have gone insane without having you to vent to).

TABLE OF CONTENTS

LIST OF TABLES

LIST OF FIGURES

SUMMARY

The purpose of this study is to create a laboratory-scale internal wave apparatus to generate a standing internal wave that mimics conditions found *in situ* for the purpose of understanding the bio-physical interactions in zooplankton habitat near the pycnocline. Internal waves, formed in regions of high temperature and salinity differences, are ubiquitous features found in many marine and freshwater ecosystems. Such waves are formed when the interface between water bodies, called the pycnocline, is oscillated. Often the pycnocline is associated with the formation of "thin layers", which are patches of high phytoplankton densities in a narrow region of the water column and the aggregation of copepod and zooplankton. Recent observations indicate that copepods and other zooplankton aggregate around internal waves.

A standing internal wave in a two-layer stratification system was theoretically analyzed to determine the expressions governing the wave motion. A boundary value problem assuming incompressible and irrotational flow was used with boundary conditions applied at the bottom, the interface between the two layers, and the free surface for kinetic and dynamic conditions. The expressions were linearized by using the small-amplitude assumption, which yielded equations describing the dispersion relation, interface locations, velocity potentials, and velocities using independent variables such as the density jump, wave number, seiching mode, and wave period.

Using the expressions, three cases with different physical arrangements were specified to test in the apparatus. These cases correspond to density jumps of 0.75, 1.0, and 1.5 σ_t. The flows were characterized using flow visualization and signal processing of the interface location. Cases 2 and 3 ($\Delta\rho = 1.0$ and 1.5 σ_t) generated a clean

standing internal wave that matched target wave parameters. In contrast, for Case 1 ($\Delta\rho = 0.75\ \sigma_t$) inconsistent wave heights were observed and non-linear waves of higher modes were generated (by forcing a high harmonic mode number).

Copepod behavioral assays were conducted for Case 2 with a density jump of 1.0 σ_t using a mixed population of Calanoid copepods *Acartia tonsa*, *Temora longicornis*, and *Eurytemora affinis*. For this density jump, copepod behavior assays were conducted in three different treatments: control (stagnant homogeneous fluid), stagnant density jump interface, and internal wave flow. When exposed to the stagnant density jump interface, the copepods reacted by showing preferential horizontal swimming motion parallel to the interface. The copepods exhibited a unique swimming behavior when exposed to the internal wave treatment. They swam in orbital-like trajectories in and around the internal wave region. The copepods also showed an affinity to the interface by preferentially swimming closer to it during the internal wave treatment compared to the other two treatments, suggesting either physical transport by the wave or behavioral response to the hydrodynamic cues. Further investigation of the trajectories of passive, neutrally-buoyant particles in the internal wave flow revealed a large contrast between the copepods' motions and the passive advection in the internal wave flow. Thus, the conclusion is that behavior plays a substantial role to explain the observed orbital-like copepod trajectories in and around the internal wave.

CHAPTER I

INTRODUCTION

Internal waves are gravity waves that oscillate within the water column, rather than on the surface. Internal waves are ubiquitous phenomena that have been studied by many ocean scientists for the past century. Internal waves are often formed in regions of high temperature or salinity variability [Phillips 1969] as the interface between the water bodies, called the pycnocline, is oscillated to create the wave. Interests in studying internal waves have varied across a wide spectrum including breaking internal waves, shoaling internal waves, and tidal internal wave packets (Thorpe 1999; Troy and Koseff 2005; Hult et al. 2009, 2011a, 2011b).

In addition to interest in the physical aspects of internal waves, often studies are focused on trying to understand the vertical mixing of nutrients or vertical displacements of plankton distributions. The pycnocline is very important for the distribution of biomass along the water column. Field observations have shown that "thin layers," which are high densities of phytoplankton biomass in sparse patches in the water column (Holliday et al. 2003), are often formed around the pycnocline (Dekshenieks et al. 2001; McManus et al. 2003). Further, copepods and other zooplankton have been observed to aggregate around thin layers (Cowles et al. 1998; Dekshenieks et al. 2001; Gallager et al. 2004; McManus et al. 2005; True 2014). Copepod and zooplankton aggregations also have been observed around internal waves *in situ* (Haury et al. 1979; Lennert-Cody and Franks 1999, 2002; Cheriton et al. 2009). Understanding the bio-physical coupling and the role of fine-scale hydrodynamic cues induced by internal waves is critical in the study of the dynamics of thin planktonic layers. The oscillations of the internal wave generate dynamic hydrodynamic cues that copepods

may be able to sense. The detection of such cues are important for copepods since aggregation around oceanic physical features dictates habitat partitioning, prey and predator interactions, and mate interactions (Woodson 2005; True 2014). However, no study to date has examined the mechanist link between the hydrodynamic flow of internal waves and copepod behavior.

In this study, we designed and constructed a laboratory-scale internal wave generator to study the biological and physical forcing at an individual scale with the intent of providing insight to the mediating factors that dictate organism distributions such as velocity, velocity and density gradients, passive settling of phytoplankton, and phytoplankton activities. First, theoretical analysis of a two layer density stratified system is provided with the purpose of guiding and defining target flow parameters. Second, the apparatus was tested for various cases of wave parameters of a standing internal wave that mimics *in situ* conditions. Third, behavior assays on marine copepods (mixed population of *Acartia tonsa, Temora longicornis* and *Eurytemora affinis*) were conducted for various physical arrangements. The trajectories of the fluid motion and copepod motion were recorded and digitized to analyze individual response to the internal wave treatment.

CHAPTER II

LITERATURE REVIEW

The purpose of this chapter is to review thin layers and internal waves, as well as the coupling of the two in the context of calanoid copepod behavior. First, thin layers are discussed in order to introduce the oceanographic structure around which zooplankton are known to aggregate. Secondly, the physical properties of internal waves are explained to characterize the flow structure that will be used in the study. Third, the bio-physical coupling at thin layers and internal waves are presented to provide information on copepod behavior in the context of foraging and aggregation.

2.1 Thin Layers

Large concentrations of phytoplankton biomass in thin vertical patches called "thin layers" (Holliday et al. 2003) have become a well-studied phenomena in the last two decades due to improvements in resolution and speed of sampling technologies (Woodson 2005). Thin layers are found in nearly all marine environments, including fjords, river mouths, continental shelves, and shelf basins (Bjornsen and Nielsen 1991; Cowles and Desiderio 1993; Cowles et al. 1993; Gentien et al. 1995; Johnson et al. 1995; Widder 1997; Dekshenieks et al. 2001; McManus et al. 2003). In these layers, spatially dense marine plankton patches are created with vertical thickness ranging from orders of *centimeters* to *meters*. They can stretch horizontally for *kilometers* and can last for days (McManus et al. 2005). The biomass found in thin layers are several orders of magnitude greater than those found in the water column above and below (McManus et al. 2005), and these aggregation of zooplankton are often correlated to physical and biological water column structure (Dekshenieks et al. 2001). The dense layers of biological activity in thin layers are indicative of the health and liveliness of

the ecosystem (True 2014). Understanding the link between individual behavior at fine scales ($< 1\ m$) and physical hydrodynamic cues is critical in defining the *in situ* conditions observed in animal distributions (Cowles et al. 1998; Gallager et al. 2004; McManus et al. 2005; True 2014).

2.1.1 Physical Properties of Thin Layers

Thin layers can be quantified through physical and biological factors which can both enhance and disperse thin layers. The enhancing factors (convergent processes) must be greater than the dissipating factors (divergent processes) in order to encourage formation of a stable layer (McManus et al. 2003; Stacey et al. 2007; Birch et al. 2008; Sullivan et al. 2010). Similarly, the two processes must be in balance for the maintenance of the layer; otherwise, the divergent factors will dissipate the layer (Sullivan et al. 2010). Both convergent and divergent processes have physical, biological, and chemical implications. The physical convergent processes include velocity and velocity gradients (shear strain rates) and density jumps. Some of the physical divergent processes are regional winds, convective overturns, and passage of non-linear waves packets (Sullivan et al. 2010). The biological and chemical processes include passive settling of phytoplankton on a pycnocline, phytoplankton activities (e.g., migration), behavioral response to chemical cues, and foraging.

Field observations have shown that thin layers are most often formed in the pycnocline (Dekshenieks et al. 2001; McManus et al. 2003). The Richardson number quantifies the feasibility of layer formation. The Richardson number (Ri) is a dimensionless number that expresses the balance between the buoyancy force and the flow gradient term [Kundu et al. 2011]. The buoyancy force represents the stabilizing effect from the vertical density stratification, and the flow gradient term represents the destabilizing effect from vertical shear. It is defined as:

$$Ri = \frac{N^2}{\left(\frac{\partial u}{\partial z}\right)^2} \tag{2.1}$$

where N is the Brunt-Väisälä stability frequency, or buoyancy frequency, defined as

$$N(z) = \sqrt{-\frac{g}{\rho_o}\frac{\partial \bar{\rho}}{\partial z}} \tag{2.2}$$

Many studies indicate that Ri must be greater than 0.25 for thin layers to exist (Dekshenieks et al. 2001; Velo-Suarez et al. 2010) which matches the theoretical threshold necessary to maintain stability for continuously stratified flow with vertical shear [Drazin and Reid 1981]. Thus this requirement ensures a balance between maintaining stratification and suppressing turbulent mixing in the layer.

Other factors in enhancing thin layer formation and maintenance include the phytoplankton's ability to maintain vertical position in the thin layer by self-regulating buoyancy (Derenbach et al. 1979; Franks 1992; Alldredge et al. 2002); vertical shear generating mechanisms that vertically suppress thin layers (Franks 1995; Ryan et al. 2008); 'gyro-tactic trapping,' the biophysical mechanism coupling between phytoplankton motility and vertical shear (Durham et al. 2009); and other biological mechanisms such as algal blooms, grazing, and swimming behavior (Cowles et al. 1998; Alldredge et al. 2002; Holliday et al. 2003; True 2014). These convergent and divergent physical and biological processes compete to either maintain or dissipate the densely populated patches. In particular, Cheriton et al. (2009) indicated an important linkage between internal wave structure and the convergence and divergence of the thin layer. He showed that the passage of internal waves had a greater impact on changing the layer thickness than shear straining, cell settling velocities, and plankton motility. Thus, a holistic understanding of the linkage between the thin layers and hydrodynamic cues associated with oceanic structures is critical (Woodson et al. 2014).

2.2 Internal Waves

Internal waves are one of the three most commonly studied forms of waves in fluid mechanics, along with interface waves and compression and expansion waves

[Kundu et al. 2011]. The presence of internal waves in the ocean was first identified in the early 1900's due to the high variability of temperature and salinity in water profiles. Such variations, especially in thermoclines, at a fixed depth have aided in identifying such phenomenon [Phillips 1969]. Internal waves have been extensively studied. Specific topics of interest include: the influence of breaking internal waves on vertical mixing (Thorpe 1999; Troy and Koseff 2005; Hult et al. 2009; Hult et al. 2011a, 2011b), flow separation due to shoaling internal waves (Boegman and Ivey 2009), and the influence of tidally-generated internal wave packets on vertical displacements of plankton distributions (Haury et al. 1979). In particular, internal gravity waves of a two-layer stratification system will be discussed in greater detail.

2.2.1 Properties of Internal Waves

Internal waves are perturbations along an interface between fluids of different densities that propagate over a wide range of temporal scales (Hult et al. 2010). A two-layer stratification is commonly studied (instead of continuous stratification) because most internal wave occurrences in oceans, lakes, and the atmosphere can be idealized as a two-layer stratification (Troy and Koseff 2005). A pycnocline is formed due to temperature and salinity variations. The most common example of temperature variance is the warming of the upper layer of the ocean through solar heating (Umeyama 2002). The salinity variations can be observed in many situations such as an estuary [Fischer et al. 1979].

Internal waves are created when the pycnocline is excited and vertically displaced. A balance between the fluid inertia and restoring force (gravity) pushes the interface back to the undisturbed position [Kundu et al. 2011]. This balance causes oscillation at the interface, which propagates as a wave. Figure 2.1 shows the streamlines as the wave propagates from left to right [Mann and Lazier 1996]. The orbits indicate that the velocity magnitude decays with the distance from the interface. The individual

water particles ultimately return to their original spot since they move in a circular orbit. The orbital structures, which decrease in magnitude away from the interface, exist along the entire water column and create converging and diverging regions. The particles move in opposite directions on opposite sides of the pycnocline and thus create shear at the interface that peaks at the crest and troughs.

The shape of internal waves is dependent on the depth of the interface location. A broad-crested inverted-trochoid with narrow troughs is observed for waves near the surface, and a narrow-crested trochoid with broad troughs is observed near the bottom (Thorpe 1968a).

Internal waves are commonly seen in field observations as well (Umeyama 2002). Studies have aided in explaining interesting internal wave phenomena [Kundu et al. 2011], such as abnormally high levels of drag experienced by ships entering a Norwegian fjord [Gill 1982]. This is an example of low-salinity water (fresh river water) entering a saltier water (oceanic water) body, thereby creating a density interface. The interface is excited as ships enter the fjord, and the drag generated via the internal wave adds extra resistance to the ships' movement.

2.2.2 Properties of Standing Internal Waves

Many methods have been used to generate a standing internal wave in a two-layer stratification. An early study by Schmidt (1908) used a rocking rectangular flume to show that the measured wave period was 6% greater than the predicted values from linear Stokes theory. Other experiments included oscillating a set of wall-mounted horizontal pistons stationed at opposite ends about the interface (Thorpe 1968b); lee wave generation behind towed obstacles [Baines 1995]; surface-wave-internal-wave interactions (Hill and Foda 1996); turbulent generation of interfacial waves of the mixed-layer (McGrath et al. 1997); and tilting and relaxing of long tilting tubes

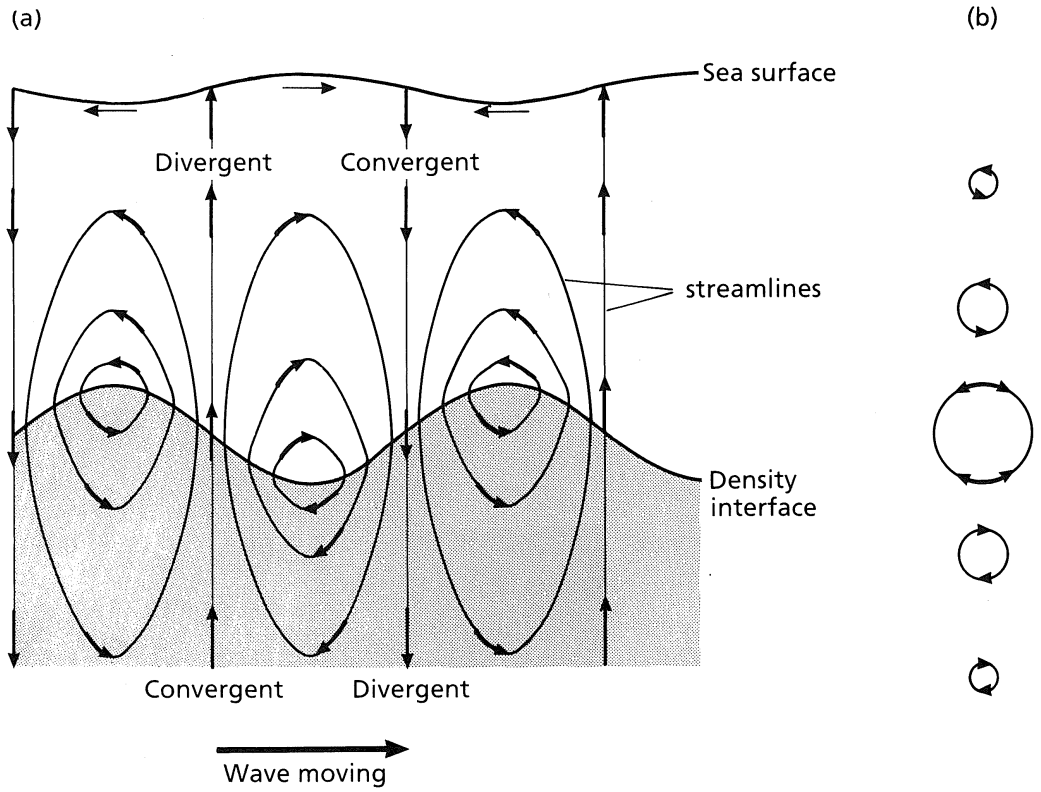

Figure 2.1: (a) An incident internal wave traveling from left to right at the density interface, showing the streamlines in the divergent and convergent zones. (b) Orbital trajectories of water particles over one wave cycle. The diameter of the trajectory decreases away from the interface. The direction of the orbit reverses at the interface indicated by the double arrows on the center orbit. (Reprinted from Mann and Lazier 1996).

(Horn et al. 2001, 2002).

Standing internal waves are created by superposing two internal waves with identical wave properties, but opposing directions. They are formed in a fixed body of water, such as a tank or a lake (standing wave in a lake is called a 'seiche'), when the incident waves are completely reflected by walls at a specific frequency [Kundu et al. 2011]. It creates a wave form that does not propagate, hence the description 'standing' [Dean and Dalrymple 1991]. A standing wave can be characterized by two types of alternating points called nodes and antinodes. The nodes are points where the interface position relative to the unperturbed location (i.e., η) is zero, and the antinodes are points where the interface reaches maximum displacement (both positive

and negative directions). The interface oscillates vertically with varying amplitude, whereas the nodes remain stationary.

A standing internal wave in a closed basin may only be created by forcing the wave at certain frequencies known as harmonics. Each harmonic is made up of $n+1$ number of nodes and n number of antinodes where n denotes the harmonic sequence (or the mode number). The wavelength is defined as $\lambda = \frac{2L}{n}$, where L is the length of the container.

Early studies by Thorpe (1968b) analyzed and described the wave shapes for various water depths at small density differences for standing internal waves in a two-layer stratification system. The water regime is divided into three zones (shallow, intermediate, and deep) in order to categorize a body of water based on its relative depth, where the relative water depth is the wave number (k) times the water depth (h). This categorization allows certain assumptions to be made depending on the regime. Shallow water corresponds to the relative water depth becoming much smaller than the wavelength ($kh < \frac{\pi}{10}$) but may be similar to the wave amplitude (in terms of orders of magnitude). Deep water corresponds to when the water depth is much greater than the wavelength ($kh > \pi$) [Svendsen 2006]. Thorpe (1968b) used both theoretical and experimental results to explain the wave profiles in various conditions, three of which are described here: (i) both layers are in deep water; (ii) upper layer is in deep water and lower layer is in shallow water; and (iii) upper layer is in shallow water and lower layer is in deep water. The density differences were kept under 0.03 g/cc for all the experiments.

In case (i), the theory showed that the shape of the wave was vertically symmetrical with no cresting. The shape was flattened at the peaks when using finite or small perturbation amplitudes. The experimental results, Figure 2.2, showed good agreement with the theory in that the wave profile was sinusoidal and was flattened at the crests and troughs. In case (ii), the theory showed an asymmetrical profile that

revealed nonlinear-wave-like cresting when moving upwards and never completely flattened. In the experimental results, Figure 2.3, the profile differed for varying amplitudes. At small perturbation amplitudes the wave behaved sinusoidally, but the profile showed upwards cresting with increase in amplitude. The profile also never returned to completely flat at the instance of minimum displacement between maximum crest and trough (Figure 2.3b). In case (iii), Figure 2.4, the theory and the experimental result showed an inverted version of case (ii).

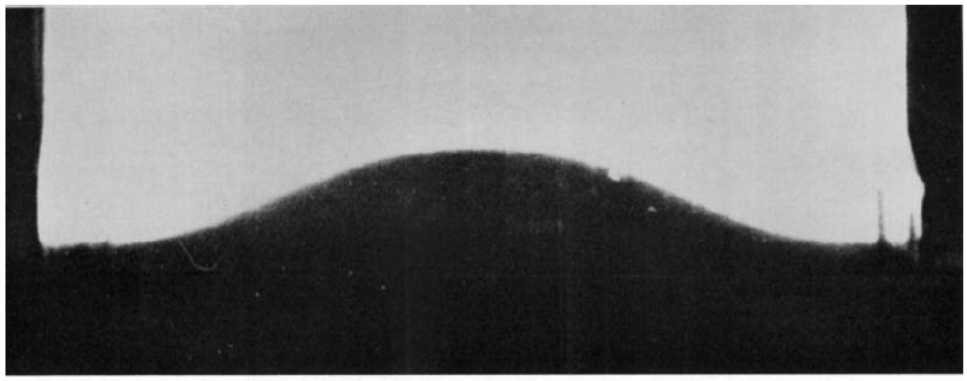

(a)

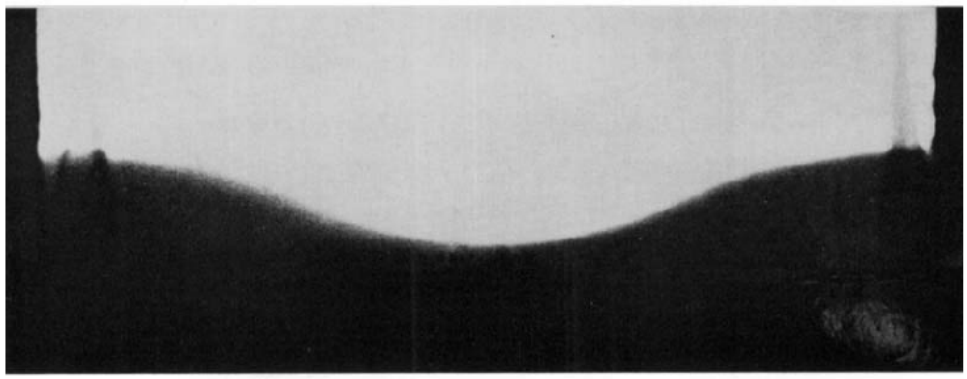

(b)

Figure 2.2: Interfacial waves between deep fluids (case i). Mode $n = 2$, $h_1 = 25.5$ cm, $h_2 = 19.0$ cm, $\Delta\rho = 9.0 \times 10^{-3}$ g/cc. (a) Maximum upward displacement; (b) maximum downward displacement. (Reprinted from Thorpe 1968b).

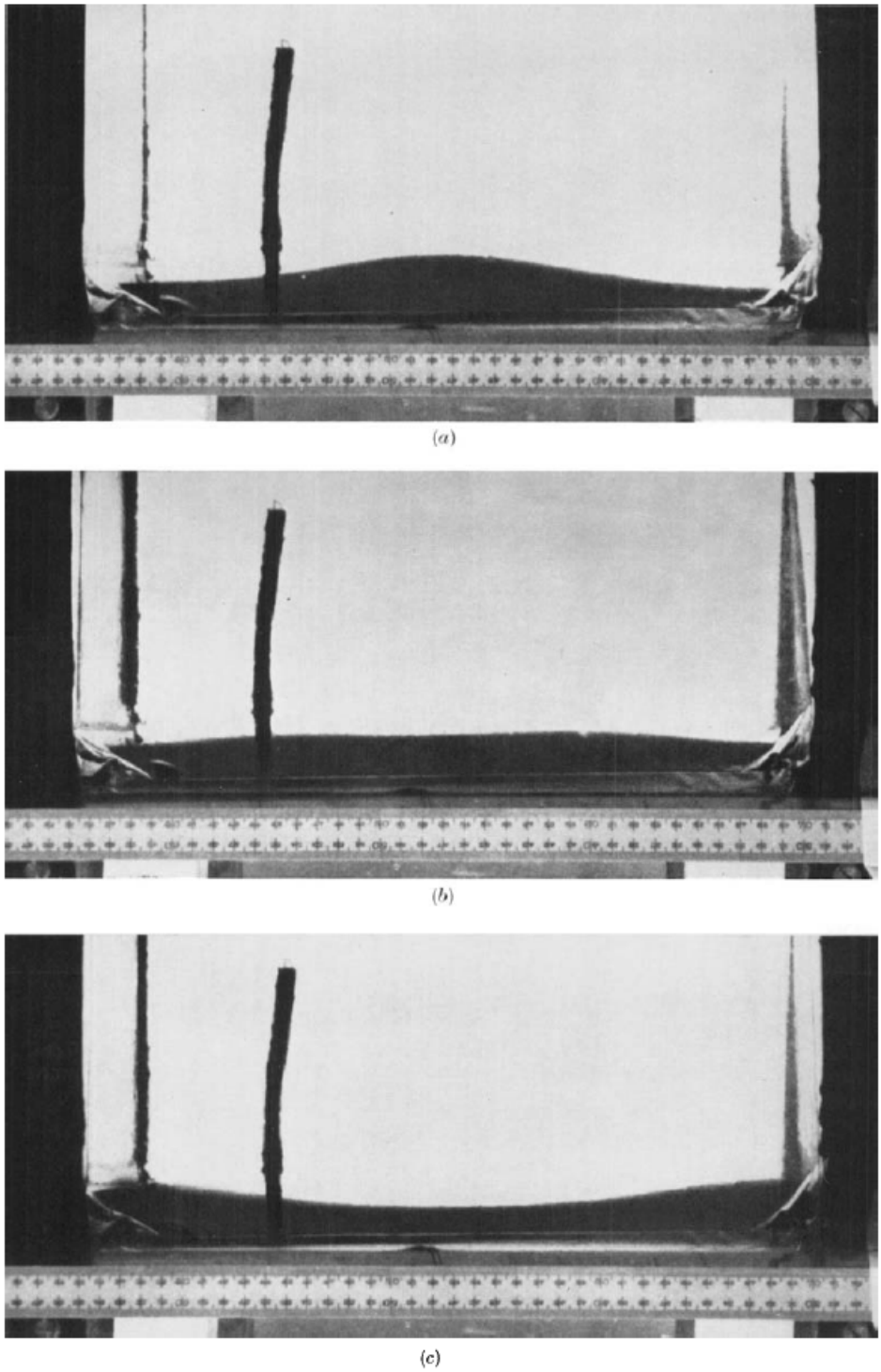

Figure 2.3: Interfacial waves in shallow lower fluid (case ii). Mode $n = 2$, $h_1 = 27.5$ cm, $h_2 = 2.7$ cm, $\Delta\rho = 19.8 \times 10^{-3}$ g/cc. (a) Maximum upward displacement; (b) minimum displacement; (c) maximum downward displacement. (Reprinted from Thorpe 1968b).

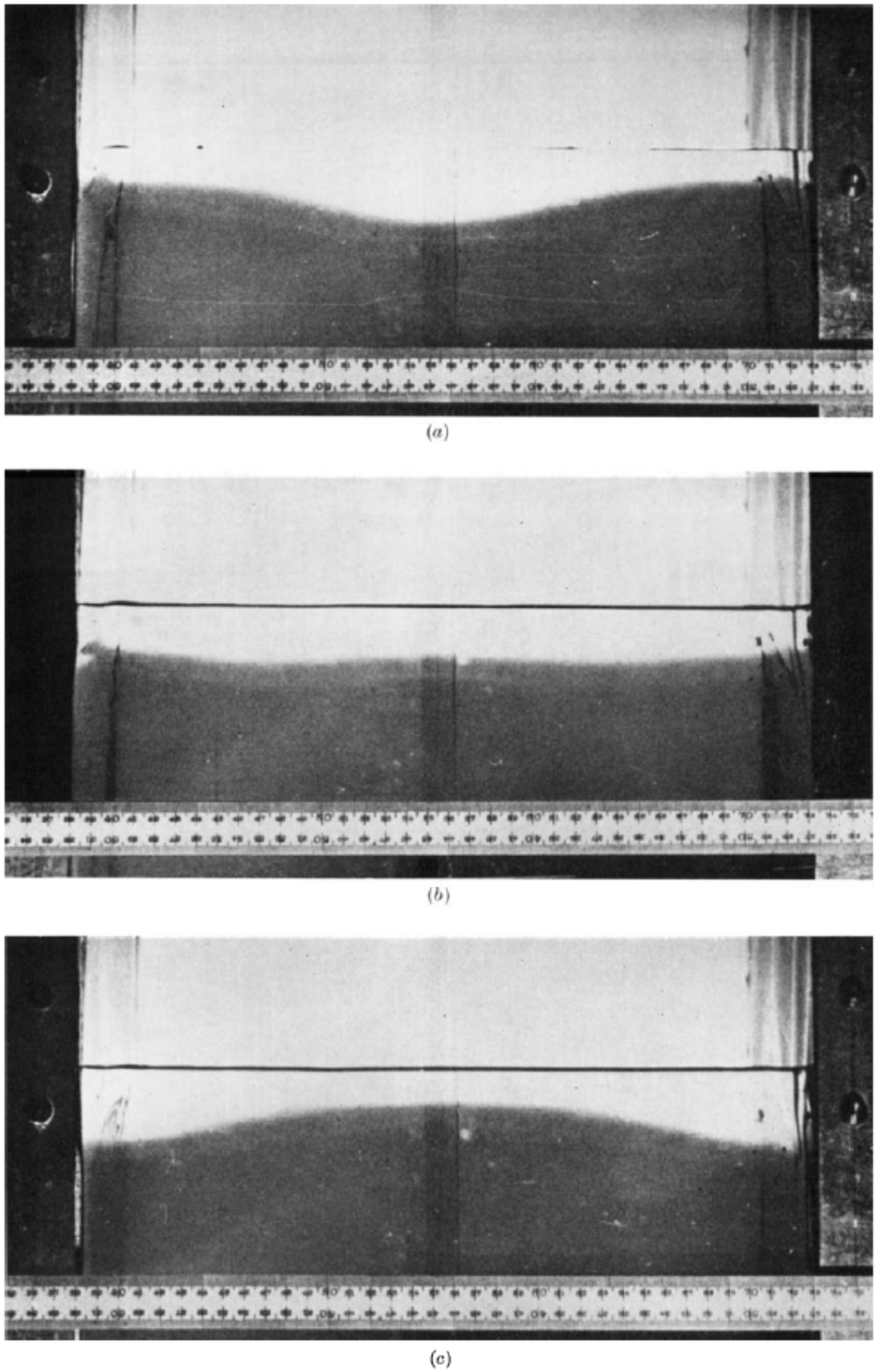

Figure 2.4: Interfacial waves in shallow upper fluid (case iii). Mode $n = 2$, $h_1 = 2.7$ cm, $h_2 = 23.0$ cm, $\Delta\rho = 15.5 \times 10^{-3}$ g/cc. (a) Maximum downward displacement; (b) minimum displacement; (c) maximum upward displacement. (Reprinted from Thorpe 1968b).

2.3 Biophysical Coupling at Thin Layers and Internal Waves

Thin layers and internal waves are ubiquitous oceanic features that affect plankton ecosystems. Most studies to date have been focused on large-scale biomass and wave structures in an effort to understand the connection between the physical forcing and the corresponding individual behavioral response. However, with recent advances in sampling methods and higher resolution optical instrumentation (Cheriton et al. 2009), there is a need for fine-scale understanding of thin layers and internal wave biophysical coupling. More importantly, quantifying the behavioral response of zooplankton to physical factors induced by internal waves typical of *in situ* conditions is critical to achieve a foundational knowledge of thin layer dynamics.

The effects of large amplitude internal waves on thin layer dynamics is a topic that has been studied in much detail (Haury et al. 1983; Lennert-Cody and Franks 1999, 2002; Vázquez et al. 2008; Lai et al. 2010; Kaartvedt et al. 2012; Haren 2014). Lennert-Cody and Franks (1999, 2002) analyzed plankton patchiness in high-frequency, large-amplitude internal waves using theoretical and idealized models and by analyzing chlorophyll fluorescence levels. The studies concluded that plankton experience changes induced by internal waves that may cause along-isopycnal blooms on the scale of 100's of meters in the cross-shore direction and that the patchiness associated with high-frequency internal waves may also be found in lakes. In a study by Kaartvedt et al. (2012), fish were studied to understand their vertical migration due to internal waves. The study concluded that the observed fish migration was a response to light intensity fluctuations caused by oscillating turbid surface layer from varying amplitudes of internal waves.

2.3.1 Significance of the Biophysical Coupling

The importance of physical and biological features, such as thin layers and internal waves, on the *in situ* patterns of animal patchiness is indicative of the observations

of enhanced biological activities in thin layers with physical velocity and density gradients (Cowles 2004; Gallager et al. 2004; McManus et al. 2005). The passage of internal waves play an important role in thin layers through vertical mixing in shelf seas (Stevens et al. 2012). In a study by Cheriton et al. (2009), vertical oscillation from the passage of internal wave had the largest impact on thin layer thickness compared to other convergent factors such as shear straining, cell settling velocities, and plankton motility. Thus in order to correctly outline the convergence and divergence processes that governs the formation, maintenance, and dissipation of thin layers, consideration of internal waves is essential.

Advances in acoustic sampling technology have allowed scientists to conduct field studies to observe the relationship between thin layers of plankton and the physical water column structures (Cheriton et al. 2009). Dekshenieks et al.'s (2001) field study of thin layers in a North Pacific fjord utilized the high-resolution sampling tool to observe a decrease in organism transport rate within the thin layer about the pycnocline. This was a response to the horizontal stretching of the thin layer induced by shear from internal waves, which also matched the numerical model developed by Franks (1995).

2.3.2 *In Situ* Conditions

Although limited, *in situ* conditions that quantify this physical and biological structure is paramount in understanding the relative fine-scales that the planktons can sense.

The field data gathered by McManus et al. (2005) Rinke et al. (2007), Vázquez et al. (2008), Cheriton et al. (2009), and Kaartvedt et al. (2012) are shown in Table 2.1. The thin layer was characterized by the density or salinity range of the layer while the internal wave was described by the wave amplitude, current velocity, wave period, and the shear strain.

Table 2.1: Summary of the *in situ* observations of thin layer and internal wave characteristics at various locations. The table includes the data source, fluid density, fluid salinity, wave amplitude, current velocity, wave period, and shear strain rate.

Author	**Location**	**Density**	**Salinity**	**Amplitude**	**Current Velocity**	**Wave Period**	**Shear Strain Rate**
Kaartvedt et al. 2012	Coast of Namibia	1026-1027.5 $kg\ m^{-3}$	-	60-80 m	-	-	-
Vázquez et al. 2008	Strait of Gibraltar	-	36.6	$> 100\ m$	$1\ m\ s^{-1}$	-	-
Rinke et al. 2007	Bautzen Reservoir (Germany)	-	-	Up to 4 m	Horizontal: 5-8 $cm\ s^{-1}$ Vertical: 4-12 $mm\ s^{-1}$	-	-
Cheriton et al. 2009	Monterey Bay	-	-	Avg. 5.7 m	-	9-13 min	$\sim 0.06\ s^{-1}$
McManus et al. 2005	Monterey Bay	-	-	-	$< 6\ cm\ s^{-1}$	18-20 min	Avg. 0.03830 s^{-1}

The data collected by Vázquez et al. (2008) was taken during spring tide when the inflow dominated the tidal currents. The inflow acted as a convergent factor by reducing the intensity of the tidal currents which acted as a divergent factor; thus, showed similar effects as the internal wave processes. The field studies in Monterey Bay (McManus et al. 2005; Cheriton et al. 2009) measured the maintenance and fluctuations of the thin layer. McManus et al. (2005) documented the average thickness of zooplankton layers to be 1.01 m and found that no layers formed for Richardson number below 0.25 due to the instability of the water column (Mann and Lazier 1996), which matched our previous understanding of this threshold. Vertical patchiness of thin layers were recorded to establish a biophysical understanding. The results showed strong statistical data to support the association: 62% of the thin layers were around the pycnocline. Zooplankton layers persisted only during the day and dissipated during the night. The layer thickness ranged from 30 cm to 4 m, and the persistence time ranged from 1 h 45 min to 15 h 30 min with an average time of 8 h 12 min. Most of the layers formed in presence of moderate shear (0.025 to 0.05 s^{-1}) with the average shear of 0.038 s^{-1}. The zooplankton seemed to aggregate around regions of little (< 6 cm s^{-1}) to no flow within the layer. McManus et al. (2005) also concluded that even at maximum internal wave heights, thin layers were not dispersed: as the wave height increased, the thin layer thickness also increased.

Rinke et al. (2007) documented field data found in lakes, showing the effects of downwelling on animal behavior. In a lake with internal wave amplitudes of up to 4 m, he observed maximum horizontal currents on the order of cm s^{-1} and vertical currents on the order of mm s^{-1}. The observations were taken during downwelling, which initiated large fluctuations of zooplankton along with internal wave generation.

Woodson et al. (2005) provided an important laboratory understanding of the influence of hydrodynamic cues in zooplankton behavior around thin layer flow structure. The animals responded to the shear strain rate, and the threshold for response

(i.e., 0.025 s^{-1}) was much smaller than the response threshold to evoke an escape response. For comparison, the threshold level to evoke an escape vary among copepod species ranging from $0.4 - 26\ s^{-1}$ (Yen and Fields 1992; Fields and Yen 1997a, 1997b; Kiørboe et al. 1999; Titelman 2001; Titelman and Kiørboe 2003a; Titelman and Kiørboe 2003b; summarized in Woodson et al. 2014). In addition, the response to environment flow structure is quite distinct from an escape jump. Woodson et al. (2005, 2007a, 2007b) found that copepods responded to velocity gradients mimicking thin layer structure with an excited area-restricted search behavior (i.e., increased swimming speed and turn frequency) as part of a cue hierarchy in the search for food.

In summary, theoretical and field studies indicate that the biophysical coupling at thin layer and internal wave structure have a clear impact on the aggregation and patchiness of zooplankton. Quantifiable cues that dictate animal behaviors and describe the water column *in situ* for finite-amplitude internal waves in thin layers are still lacking in the literature. Therefore, a laboratory scale study has the potential to build a connection between the biophysical linkage of thin layers and internal waves to zooplankton ecology.

2.3.3 Calanoid Copepod Ecology

Copepods are aquatic animals found abundantly throughout both freshwater and marine environments. They are considered to be the most numerous multicellular organisms on earth. As a subclass of the phylum Crustacea, these Copepoda are divided into about 200 families, 1650 genera, and 11,500 species (Wiebe et al. 1992; Humes 1994; Mauchline 1998). Within the subclass of Copepoda, our interest lies within calanoid copepods which consists of 1800 marine species divided in 11 superfamilies. The three species used in this study all belong in the superfamily of Centropagoidea: *Temora longicornis* (Centropagoidea Temoridae), *Eurytemora affinis* (Centropagoidea Temoridae), and *Acartia tonsa* (Centropagoidea Acartiidae).

The typical body length of these zooplankton range between 0.5 to 3.0 mm and serve as a major food source for fish, krill, and whales [Mauchline 1998]. They are dominant consumers of phytoplankton (Kleppel 1993; Bronmark and Hansson 2005; Gretchen et al. 2006); thus, serving as an important subset of mesozooplankton in marine environments connecting the food chain [Mauchline 1998; Miller 2004]. Subsequently understanding how copepods interact in marine environments is critical.

The swimming styles that copepods can inhibit are shown in Figure 2.5. *T. longicornis* and *E. affinis* swim in a cruise-style pattern (Figure 2.5a), whereas *A. tonsa* exhibits a hop-sink pattern (Figure 2.5c). The cruise swimmers propel their body forward by rapidly beating a pair of cephalic appendages. *T. longicornis* typically swim at speeds between $2 - 12\ mm\ s^{-1}$ with escape velocities approaching 30 $mm\ s^{-1}$, and *E. affinis* typically exhibit swimming speeds of $2 - 5\ mm\ s^{-1}$ (Woodson 2005). *A. tonsa* swim at speeds of $1 - 4\ mm\ s^{-1}$ (Woodson 2005).

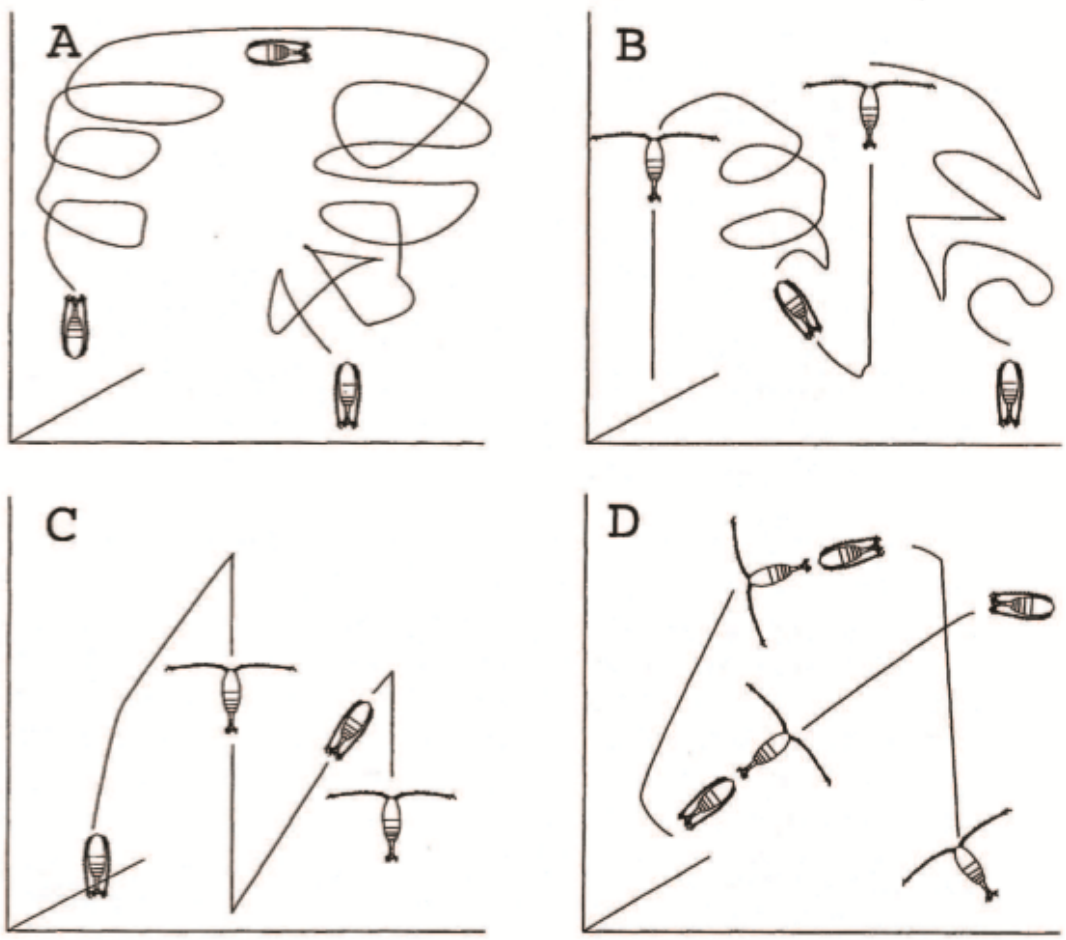

Figure 2.5: Calanoid copepod swimming styles: (a) cruising, (b) cruise and sink, (c) hop and sink, and (d) jumping. (Reprinted from Mauchline 1998).

In previous laboratory study by Woodson et al. (2007a; 2007b), the reactions of each species (*T. longicornis*, *A. tonsa*, and *E. affinis*) to density gradients have been reported. *T. longicornis* and *A. tonsa* both showed a reluctance to cross a strong density gradient (Woodson et al. 2007a). In fact, upon contact with the density gradient individuals of both species showed motion parallel to the layer or simply turning around. The density jump threshold in which both species showed change in swimming behavior is reported in Figure 2.6. Based on regression of the number of individuals crossing versus the magnitude of the density gradient, the lower and upper

threshold boundaries were $\Delta\sigma_t = 0.4$ and 2.0 for *T. longicornis* and $\Delta\sigma_t = 0.8$ and 1.4 for *A. tonsa*. The upper thresholds represent the number when approximately 75% of the tested population did not cross the layer. In contrast, *E. affinis* did not exhibit any inhibition to crossing the density jump layer (Woodson et al. 2007b). Instead, *E. affinis* showed an increase in proportional residence time under the presence of a density gradient layer, as well as an increase in swimming speed and turning frequency.

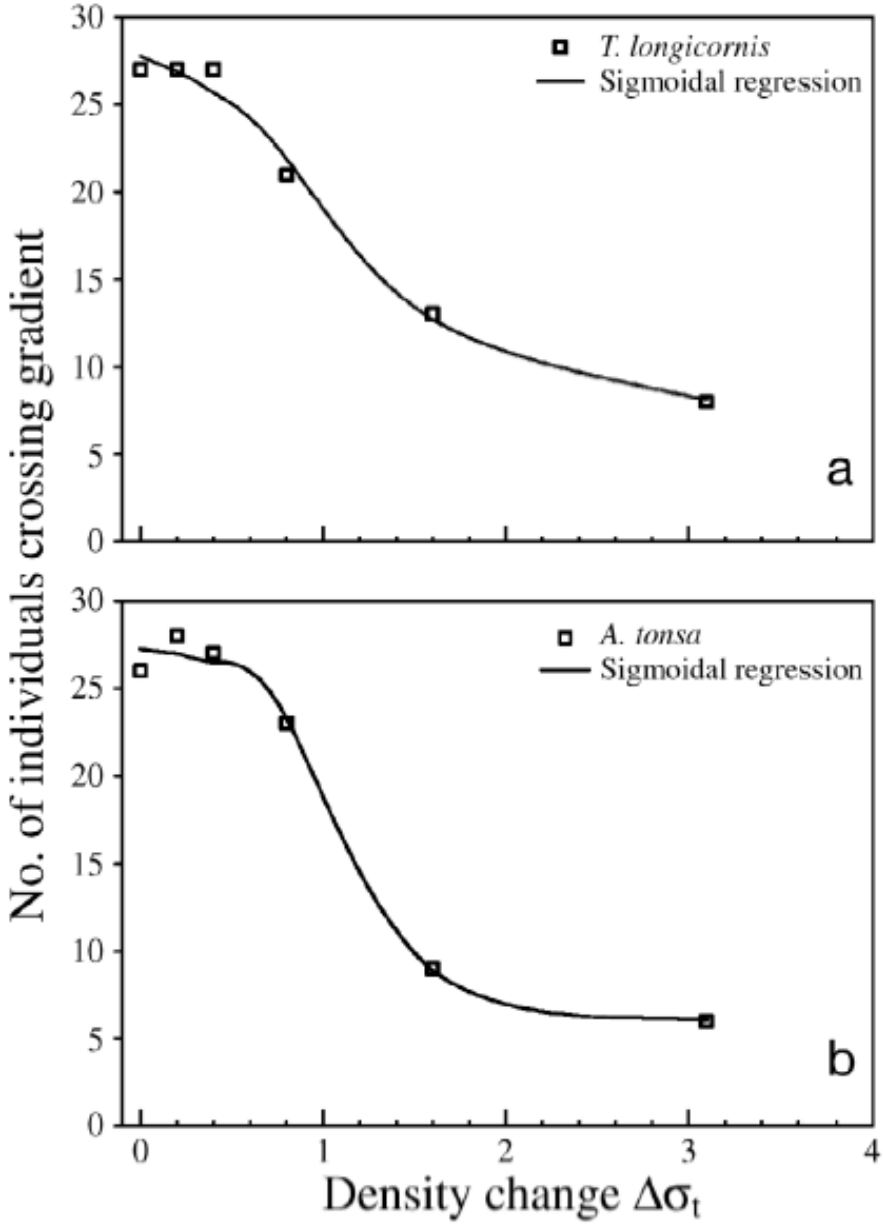

Figure 2.6: Behavioral response to the density gradient layer treatment represented as the number of individual crossing the layer. (a) *Temora longicornis* and (b) *Acartia tonsa*. The threshold levels, defined as the point where the sigmoidal curve begins to decrease, were $\Delta\sigma_t = 0.4$ and 0.8 for *T. longicornis* and *A. tonsa* respectively (Reprinted from Woodson et al. 2007a).

CHAPTER III

THEORETICAL ANALYSIS

As the initial stage of the design of the apparatus and specification of the operation parameters, theoretical considerations were taken to understand the influence of the independent variables. Figure 3.1 shows a simplified two-layer density stratified system. This system was analyzed following the techniques described in Kundu et al. [2011] and Dean and Dalrymple [1991].

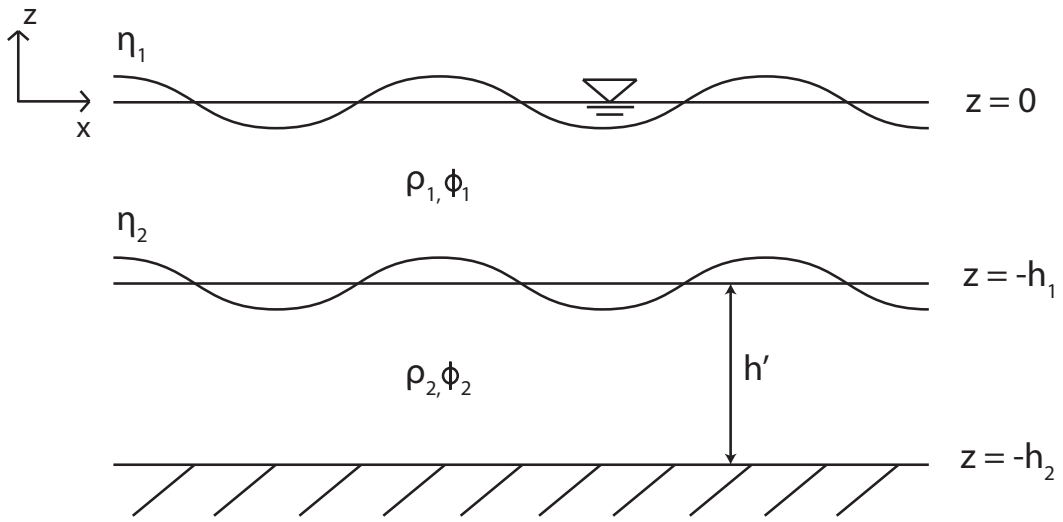

Figure 3.1: Schematic of the Boundary Layer Problem (BLP) for a two-layer stratified internal wave.

3.1 Boundary Value Problem Formulation

The vertical axis is denoted as the z-axis; $z = 0$ is at the still water depth of the upper layer, $z = -h_1$ is at the still water depth of the lower layer (or also the density interface), and $z = -h_2$ is the bottom boundary. The instantaneous surface positions (as a function of x, y, and time) of layers 1 and 2 are denoted by η_1 and η_2, which are measured from the still water levels, $z = 0$ and $z = -h_1$ respectively. The density and velocity potential are denoted by ρ and ϕ, respectively, with the subscript indicating the layer (Fig. 3.1). The thickness of the lower layer will be expressed as h' (where $h' = h_2 - h_1$) and the density difference as $\Delta\rho$ (where $\Delta\rho = \rho_2 - \rho_1$). For this system, a *Boundary Value Problem* (BVP) is established for both layers. Assuming 2-D, irrotational and incompressible flow and substituting the definition of the velocity potential into the continuity equation yields the governing equations:

$$\nabla^2\phi_1 = 0 \qquad ; \qquad -h_1 + \eta_2 \leq z \leq \eta_1 \tag{3.1}$$

$$\nabla^2\phi_2 = 0 \qquad ; \qquad -h_2 \leq z \leq -h_1 + \eta_2 \tag{3.2}$$

The boundary conditions needed to solve this BVP are listed here. BBC is the bottom boundary condition and physically corresponds to the velocity equaling zero at the solid bottom boundary. KFSBC is the kinematic free surface condition, which states that a particle on the free surface stays on the surface, $z = \eta_1$. DFSBC is the dynamic free surface condition that expresses the continuity of stress at the free surface. Assuming inviscid flow, the shear stress is zero everywhere. KIBC1 and KIBC2 are the kinematic interface ($z = -h_1 + \eta_2$) condition for the upper layer and the lower layer, respectively. Pressure 1 and Pressure 2 terms denote the pressure for the upper layer and the lower layer respectively. A comma subscript used denotes a partial derivative with respect to the coordinate following.

$$\text{BBC:} \qquad \phi_{2,z} = 0 \qquad ; \qquad z = -h_2 \tag{3.3}$$

$$\text{KFSBC:} \qquad \eta_{1,t} + \phi_{1,x}\eta_{1,x} = \phi_{1,z} \qquad ; \qquad z = \eta_1 \tag{3.4}$$

$$\text{DFSBC:} \qquad g\eta_1 + \frac{1}{2}(\phi_{1,x}^2 + \phi_{1,z}^2) + \phi_{1,t} = 0 \qquad ; \qquad z = \eta_1 \tag{3.5}$$

$$\text{KIBC1:} \qquad \eta_{2,t} + \phi_{1,x}\eta_{2,x} = \phi_{1,z} \qquad ; \qquad z = -h_1 + \eta_2 \tag{3.6}$$

$$\text{KIBC2:} \qquad \eta_{2,t} + \phi_{2,x}\eta_{2,x} = \phi_{2,z} \qquad ; \qquad z = -h_1 + \eta_2 \tag{3.7}$$

$$\text{Pressure 1:} \qquad P_1 = -\rho_1 gz - \frac{1}{2}\rho_1(\phi_{1,x}^2 + \phi_{1,z}^2) - \rho_1\phi_{1,t} \tag{3.8}$$

$$\text{Pressure 2:} \qquad P_2 = \rho_1 gh_1 - \rho_2 g(z + h_1) - \frac{1}{2}\rho_2(\phi_{2,x}^2 + \phi_{2,z}^2) - \rho_2\phi_{2,t} \tag{3.9}$$

At the interface between layers 1 and 2 ($z = -h_1 + \eta_2$), the pressure must match in order for the normal stress to be smoothly varying with no discontinuity:

$$P_1 = P_2$$

$$-\rho_1 g\eta_2 - \frac{1}{2}\rho_1(\phi_{1,x}^2 + \phi_{1,z}^2) - \rho_1\phi_{1,t} = -\rho_2 g\eta_2 - \rho_2\phi_{2,t} - \frac{1}{2}\rho_2(\phi_{2,x}^2 + \phi_{2,z}^2) \tag{3.10}$$

Next, the following scaling definitions are used to non-dimensionalize the boundary conditions and will be used to determine which terms are relatively negligible. The variables k (wave number), a (wave amplitude), and g (gravitational acceleration) are used because they provide the most appropriate relevant scales for each scaling factors:

$$x' = kx \qquad y' = ky \qquad z' = kz \tag{3.11}$$

$$\eta' = \frac{\eta}{a} \qquad \phi' = \frac{\phi k}{a\sqrt{gk}} \qquad t' = t\sqrt{gk} \tag{3.12}$$

The resulting governing equations in non-dimensional form are:

$$\nabla^2\phi_1' = 0 \qquad ; \qquad -kh_1 + ka\eta_2' \le z' \le ka\eta_1' \tag{3.13}$$

$$\nabla^2\phi_2' = 0 \qquad ; \qquad -kh_2 \le z' \le -kh_1 + ka\eta_2' \tag{3.14}$$

The resulting boundary conditions in non-dimensional form are:

$$\text{BBC:} \qquad \phi'_{2,z'} = 0 \quad ; \quad z' = -kh_2 \tag{3.15}$$

$$\text{KFSBC:} \qquad \eta'_{1,t'} + ka\phi'_{1,x'}\eta'_{1,x'} = \phi'_{1,z'} \quad ; \quad z' = ka\eta'_1 \tag{3.16}$$

$$\text{DFSBC:} \qquad \eta'_1 + \frac{1}{2}ka(\phi'^2_{1,x'} + \phi'^2_{1,z'}) + \phi'_{1,t'} = 0 \quad ; \quad z' = ka\eta'_1 \tag{3.17}$$

$$\text{KIBC1:} \qquad \eta'_{2,t'} + ka\phi'_{1,x'}\eta'_{2,x'} = \phi'_{1,z'} \quad ; \quad z' = -kh_1 + ka\eta'_2 \tag{3.18}$$

$$\text{KIBC2:} \qquad \eta'_{2,t'} + ka\phi'_{2,x'}\eta'_{2,x'} = \phi'_{2,z'} \quad ; \quad z' = -kh_1 + ka\eta'_2 \tag{3.19}$$

$$\begin{aligned}\text{Pressure:} \qquad & -\rho_1 ka\eta'_2 - \frac{1}{2}\rho_1(ka)^2(\phi'^2_{1,x'} + \phi'^2_{1,z'}) - \rho_1 ka\phi'_{1,t'} \\ & = -\rho_2 ka\eta'_2 - \rho_2 ka\phi'_{2,t'} - \frac{1}{2}\rho_2(ka)^2(\phi'^2_{2,x'} + \phi'^2_{2,z'})\end{aligned} \tag{3.20}$$

The 'ka' term denotes the steepness of the wave. In the current application, it is assumed that the wave has small amplitude compared to the wavelength; therefore, terms scaled with 'ka' are assumed to be small and are neglected. For example in the pressure equation (Equation 3.20, dynamic interface boundary condition), the leading 'ka' term is to the 2^{nd} power; thus only this term is neglected. Another major change worth noting when applying this small amplitude assumption is that η'_2 is now relatively small compared to the water depth, $-h_1$, which allows us to ignore the perturbation when considering the vertical location of our boundary conditions. As a consequence of making the small amplitude assumption, the equations are linearized.

Now, we switch back to the dimensional form of the equations by employing the small amplitude assumption. The simplified governing equations are:

$$\nabla^2\phi_1 = 0 \qquad ; \qquad -h_1 \le z \le 0 \tag{3.21}$$

$$\nabla^2\phi_2 = 0 \qquad ; \qquad -h_2 \le z \le -h_1 \tag{3.22}$$

The kinematic and dynamic boundary conditions for surface and interface are each combined to form new boundary condition equations. The surface conditions (Equations 3.24 and 3.25) are combined to create a surface equation (Equation 3.26). For the

interface conditions (Equations 3.27 and 3.28), the water surface terms are matched to yield a Kinematic Interface equation (Equation 3.29).

$$\text{BBC:} \qquad \phi_{2,z} = 0 \quad ; \quad z = -h_2 \tag{3.23}$$

$$\text{KFSBC:} \qquad \eta_{1,t} = \phi_{1,z} \quad ; \quad z = 0 \tag{3.24}$$

$$\text{DFSBC:} \qquad g\eta_1 + \phi_{1,t} = 0 \quad ; \quad z = 0 \tag{3.25}$$

$$\text{Surface:} \qquad \phi_{1,tt} + g\phi_{1,z} = 0 \quad ; \quad z = 0 \tag{3.26}$$

$$\text{KIBC1:} \qquad \eta_{2,t} = \phi_{1,z} \quad ; \quad z = -h_1 \tag{3.27}$$

$$\text{KIBC2:} \qquad \eta_{2,t} = \phi_{2,z} \quad ; \quad z = -h_1 \tag{3.28}$$

$$\text{Kinematic Interface:} \qquad \phi_{1,z} = \phi_{2,z} \quad ; \quad z = -h_1 \tag{3.29}$$

$$\text{Dynamic Interface:} \qquad \Delta\rho g\eta_2 + \rho_2\phi_{2,t} - \rho_1\phi_{1,t} = 0 \quad ; \quad z = -h_1 \tag{3.30}$$

3.2 General Solution

The general solutions for each layer are solved using the combined boundary conditions (Equations 3.23, 3.26, 3.29, and 3.30). First, the general solutions for the water surface locations and the associated velocity potentials for incident and reflective waves are as follows:

$$\eta_1 = a_1[e^{i(kx-\omega t)} + e^{i(-kx-\omega t)}] \tag{3.31}$$

$$\eta_2 = a_2[e^{i(kx-\omega t)} + e^{i(-kx-\omega t)}] \tag{3.32}$$

$$\phi_1 = [B\,cosh\,(kz) + C\,sinh\,(kz)][e^{i(kx-\omega t)} + e^{i(-kx-\omega t)}] \tag{3.33}$$

$$\phi_2 = [A\,cosh\,k\,(h_2 + z)][e^{i(kx-\omega t)} + e^{i(-kx-\omega t)}] \tag{3.34}$$

where a is the amplitude of the wave, k is the wave number , ω is the circular frequency, and A, B, and C are constants. The boundary conditions are used to solve for these

constants. By using the KFSBC (Equation 3.24) at $z = 0$, constant C is defined as:

$$C = \frac{-i\omega a_1}{k} \tag{3.35}$$

Constant B is found using the DFSBC (Equation 3.25):

$$B = \frac{-iga_1}{\omega} \tag{3.36}$$

Next, the kinematic interface boundary condition (Equation 3.29) is used to solve for constant A:

$$A = \frac{-ia_1(\frac{\omega}{k}\, cosh\, kh_1 - \frac{g}{\omega}\, sinh\, kh_1)}{sinh\, kh'} \tag{3.37}$$

Using A, B, and C, the velocity potentials ϕ_1 and ϕ_2 are redefined as:

$$\phi_1 = -ia_1(\frac{g}{\omega}\, cosh\, kz + \frac{\omega}{k}\, sinh\, kz)[e^{i(kx-\omega t)} + e^{i(-kx-\omega t)}] \tag{3.38}$$

$$\phi_2 = \left[\left(\frac{-ia_1(\frac{\omega}{k}\, cosh\, kh_1 - \frac{g}{\omega}\, sinh\, kh_1)}{sinh\, kh'}\right)\, cosh\, k(h_2 + z)][e^{i(kx-\omega t)} + e^{i(-kx-\omega t)}\right] \tag{3.39}$$

3.3 Wave Parameters

Based on the wave surface locations (Equations 3.31 and 3.32) and velocity potentials (Equations 3.38 and 3.39), various wave parameters are determined for characterizing the experimental parameters (Section 4.1.2). The wave parameters include amplitude ratio, wave dispersion, and local velocities.

3.3.1 Amplitude Ratio

The amplitude ratio is important in understanding the relationship between the wave perturbations at the two interfaces and also provides insight to the flow in the

two layers, especially when determining the local velocity terms for each layer. KIBC1 (Equation 3.27) is used to find the ratio.

$$\frac{a_2}{a_1} = \frac{k}{\omega}(\frac{\omega}{k}cosh\,kh_1 - \frac{g}{\omega}sinh\,kh_1) \tag{3.40}$$

3.3.2 Wave Dispersion

The wave dispersion relationship, which describes how a field of propagating waves separates due to the various frequencies generating different wave celerities, is critical in determining the positive and negative mode of the wave parameters. Two different modes exist because of the nature of the two-layer stratification system. To find the wave dispersion, the dynamic interface condition (pressure, Equation 3.30) is used.

$$\Delta\rho\, g a_2 + \rho_2 \frac{-ia_1(\frac{\omega}{k}cosh\,kh_1 - \frac{g}{\omega}sinh\,kh_1)}{sinh\,kh'}(-i\omega)cosh\,kh' \\ - \rho_1(-i\omega)(-ia_1)(\frac{g}{\omega}cosh\,kh_1 - \frac{\omega}{k}sinh\,kh_1) = 0$$

Dividing by a_1, substituting the amplitude ratio, and rearranging the expression yields:

$$\rho_2(g\,cosh\,kh_1 - \frac{g^2k}{\omega^2}sinh\,kh_1) - \rho_1(g\,cosh\,kh_1 - \frac{g^2k}{\omega^2}sinh\,kh_1) \\ - \rho_2(\frac{\omega^2}{k}cosh\,kh_1 - g\,sinh\,kh_1)coth\,kh' + \rho_1(g\,cosh\,kh_1 - \frac{\omega^2}{k}sinh\,kh_1) = 0$$

After factoring, dividing by $g\,sinh\,kh_1$, multiplying by $\frac{\omega^2}{gk}$, and rearranging we arrive at the final form of the expression:

$$\left(\frac{\omega^2}{gk}coth\,kh' - 1\right)\left(\rho_2\frac{\omega^2}{gk}coth\,kh_1 - \rho_2 + \frac{\rho_1(\frac{\omega^2}{gk}+1)(\frac{\omega^2}{gk}-1)}{(\frac{\omega^2}{gk}coth\,kh' - 1)}\right) = 0 \tag{3.41}$$

This equation shows two roots (i.e. solutions for ω), meaning that there are two possible modes for the dispersion relationship. The terms in the left parenthesis show mode 1, which acts as a barotropic surface wave, to be

$$\omega^2 = gk\,tanh\,kh' \tag{3.42}$$

To solve for the second mode of dispersion, the terms in the right parenthesis are rearranged to form a quadratic-like function.

$$0 = \left[\frac{\rho_1}{g^2k^2} + \frac{\rho_2}{g^2k^2}coth(kh_1)coth(kh')\right]\omega^4 + \left[-\frac{\rho_2}{gk}coth(kh_1) - \frac{\rho_2}{gk}coth(kh')\right]\omega^2 + [\rho_2 - \rho_1]$$

By treating this as a quadratic equation, the dispersion relationship for the second mode yields a positive and negative mode. The mode name follows the sign that proceeds the square root term in Equation 3.43. The positive mode yields values that are too small. For example, the wave period for a density jump of 1 σ_t at a seiching mode of 12 is 0.52 *seconds* which corresponds to a wavelength of 9.2 *mm*. The negative mode yields a more reasonable value, and therefore is the mode of interest:

$$\omega^2 = \frac{-b \pm \sqrt{b^2 - 4ac}}{2a} \tag{3.43}$$

where

$$a = \frac{1}{g^2k^2}\left(\rho_1 + \rho_2\, coth(kh_1)coth(kh')\right)$$

$$b = -\frac{\rho_2}{gk}\left(coth(kh_1) + coth(kh')\right)$$

$$c = \rho_2 - \rho_1$$

3.3.3 Local Velocities

The local velocity at every point in space needs to be quantified to construct a velocity field for copepod behavioral analysis. The local velocities in the x and y directions for both layers are calculated using the definition of the velocity potential

function.

$$u_1 = \frac{\partial \phi_1}{\partial x} = -2a_1 k \left[\frac{g}{\omega}\, cosh(kz) + \frac{\omega}{k} sinh(kz)\right] sin(kx) sin(-\omega t) \tag{3.44}$$

$$w_1 = \frac{\partial \phi_1}{\partial z} = 2a_1 k \left[\frac{g}{\omega}\, sinh(kz) + \frac{\omega}{k} cosh(kz)\right] cos(kx) sin(-\omega t) \tag{3.45}$$

$$u_2 = \frac{\partial \phi_2}{\partial x} = -2a_1 k \left(\frac{\frac{\omega}{k} cosh\, kh_1 - \frac{g}{\omega} sinh\, kh_1}{sinh\, kh'}\right) cosh\, k(h_2 + z) sin(kx) sin(-\omega t) \tag{3.46}$$

$$w_2 = \frac{\partial \phi_2}{\partial z} = 2a_1 k \left(\frac{\frac{\omega}{k} cosh\, kh_1 - \frac{g}{\omega} sinh\, kh_1}{sinh\, kh'}\right) sinh\, k(h_2 + z) cos(kx) sin(-\omega t) \tag{3.47}$$

Figures 3.2 and 3.3 shows the interface profile envelope and the incident and reflected theoretical, maximum velocity vectors for a two-layer density stratification system (based on the equations derived above). The figures show the velocity field of the negative mode. As expected, the velocity magnitude decays with distance from the interface. The vertical velocities are maximum at the antinodes and zero at the nodes, whereas the horizontal velocities are maximum at the nodes and zero at the antinodes. Also, the velocity is equal in magnitude but opposite in direction at the interface which physically matches to the boundary conditions applied.

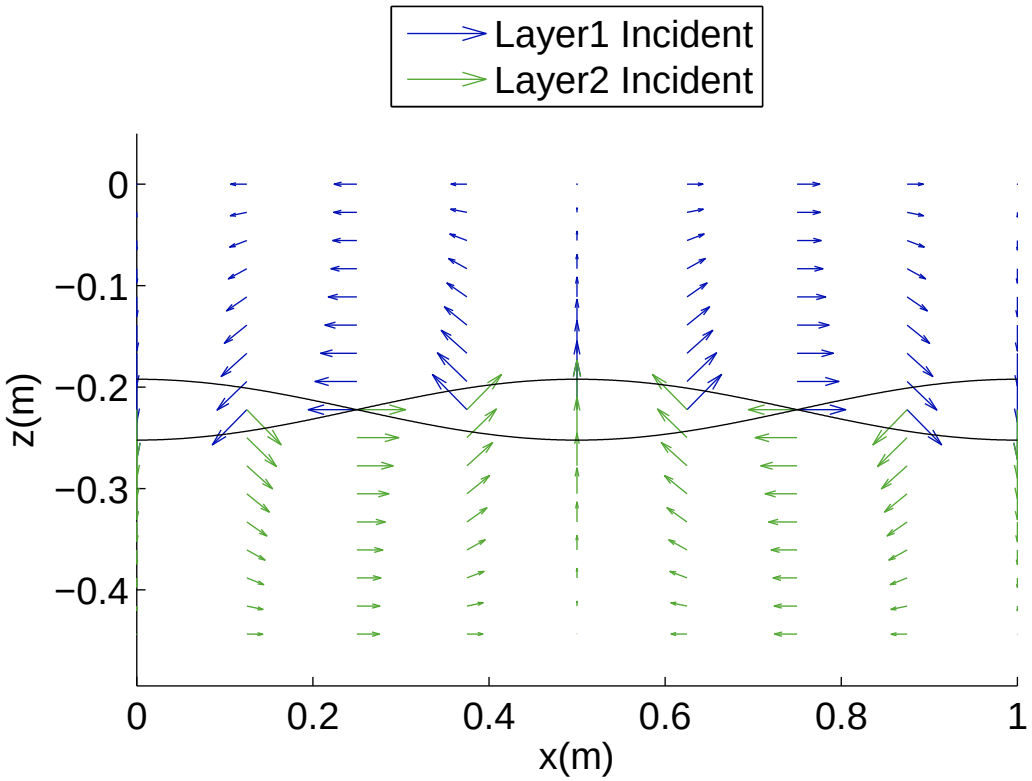

Figure 3.2: Interface envelope (black line) of the standing internal wave and the maximum velocity vectors of the incident waves for a two-layer density stratification system.

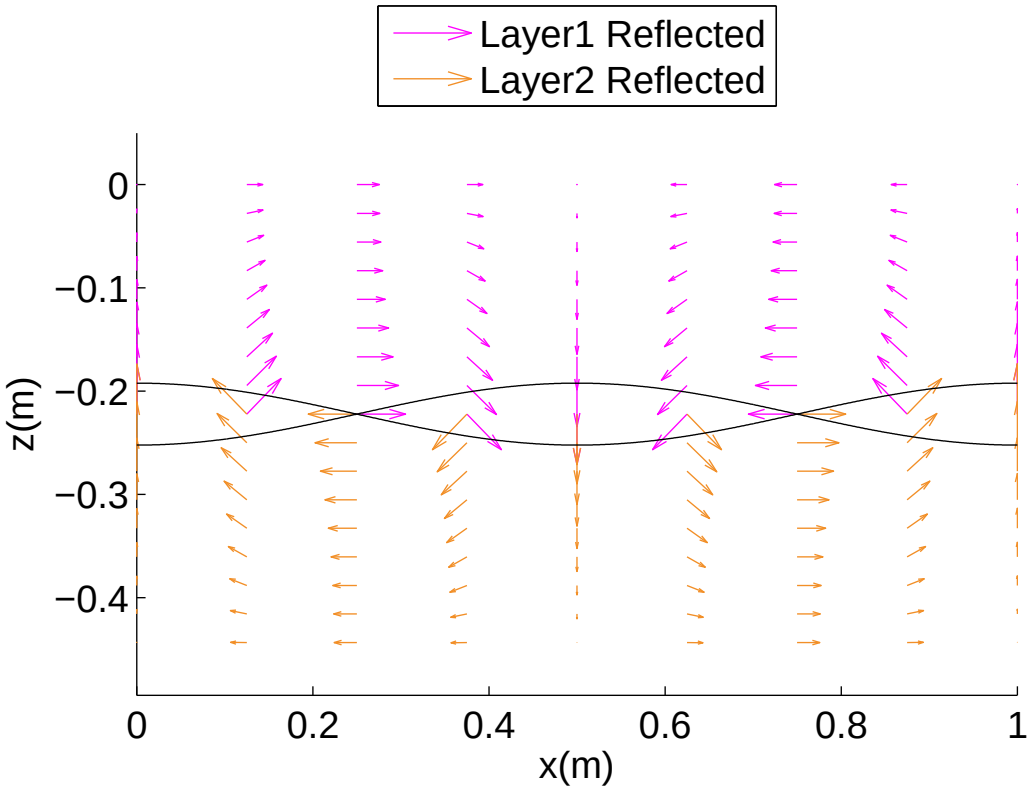

Figure 3.3: Interface envelope (black line) of the standing internal wave and the maximum velocity vectors of the reflected waves for a two-layer density stratification system.

CHAPTER IV

METHODS

The experiments in this study aimed to provide insight to the bio-physical interaction and the role of fine-scale hydrodynamic cues induced by internal waves on zooplankton distributions. The research has two main components: flow characterization and marine copepod behavioral assays both in a newly-constructed internal wave apparatus. A laboratory-scale internal wave apparatus was created to replicate the flow characteristics of a standing internal wave in a two-layer stratification system *in situ*. Three cases with different wave properties were tested. The target parameters were chosen based on analytical analysis of a standing internal wave in a two-layer stratified system. Flow visualization and signal processing were used to quantitatively and qualitatively compare the results to the target parameters. Copepod behavioral assays were conducted to understand their response to hydrodynamic cues associated with internal waves such as fluid density gradients and velocity gradients (quantified as shear deformation rate).

4.1 Experimental Design

The main tank (2.5 m $\times$ 50 cm $\times$ 50 cm) was constructed from clear acrylic sheets with thickness of 1.905 cm (Figure 4.1). The recirculating flow system used in previous studies of horizontal and vertical thin layers (True 2014; Woodson et al. 2005) was used to fill the main tank with a two-layer stratification. The reservoir used to fill the main tank consisted of two connected tanks (32 *gallon*, Rubbermaid Brute). Water was pumped to a constant head tank by using a 4-diaphragm, positive

displacement pump (JABSCO Industrial Diaphragm Pump model 31801-0115). The elevated constant-head tank (28 L, US Plastics) with a free surface was used to provide a source of steady potential energy. An overflow line from the constant head tank to the reservoir provided the recirculation needed. The constant head tank drove flow through a flow-meter (King Instrument Co., range 0 19 L/min [0 - 5 GPM]) and a line diffuser at a maximum of 7.6 L/min. Using the constant head tank alleviated potential problems of unsteady pressure perturbation and pump heating of the incoming fluid. As shown in Figure 4.2, the diffuser was installed along the middle of the tank floor by connecting a plumbing-T-fitting and a fabricated PVC (schedule 40) bushing to fit a 1.905 cm hole through the tank floor. The line diffuser (schedule 40 PVC pipe) had a total of 60 holes, each with a diameter of 0.254 cm. The holes were placed in pairs 15 cm apart and each pair was offset 45 degrees from the vertical axis to form a pair of downward laminar flow jets (Figure 4.2).

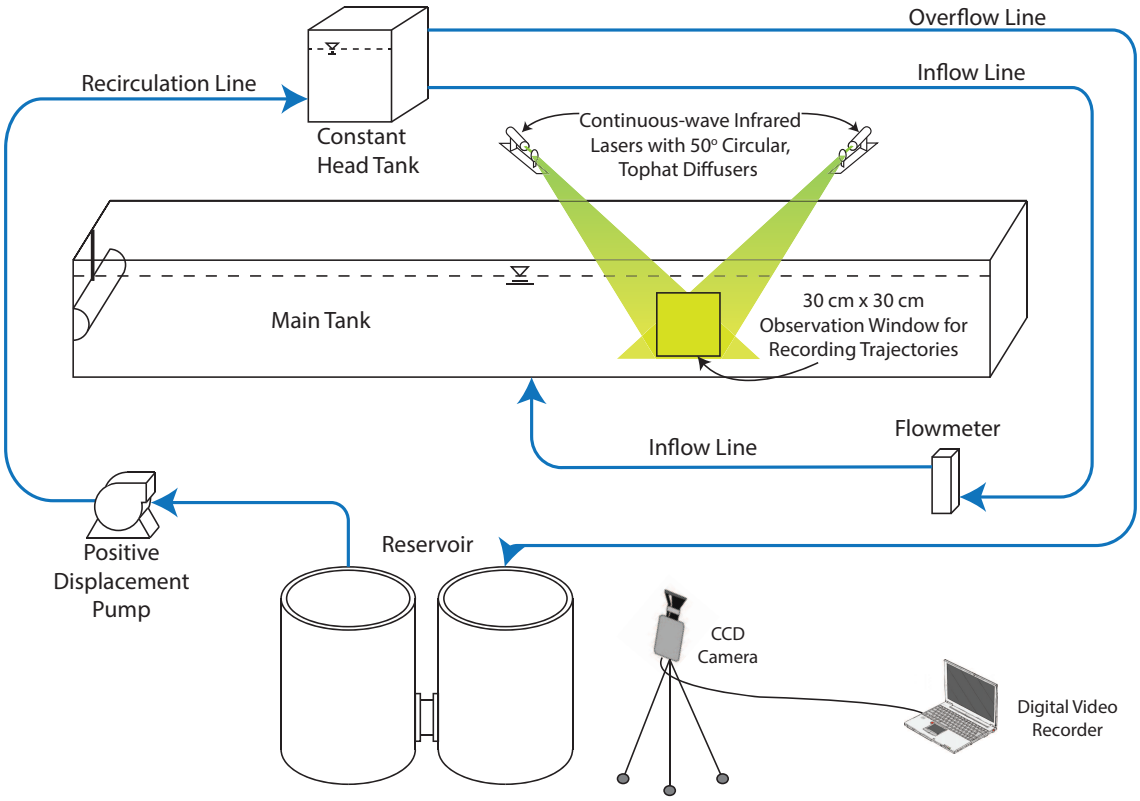

Figure 4.1: Schematic diagram of the recirculating filling system. Also shown is the optical equipment configuration employed for the copepod behavior assays.

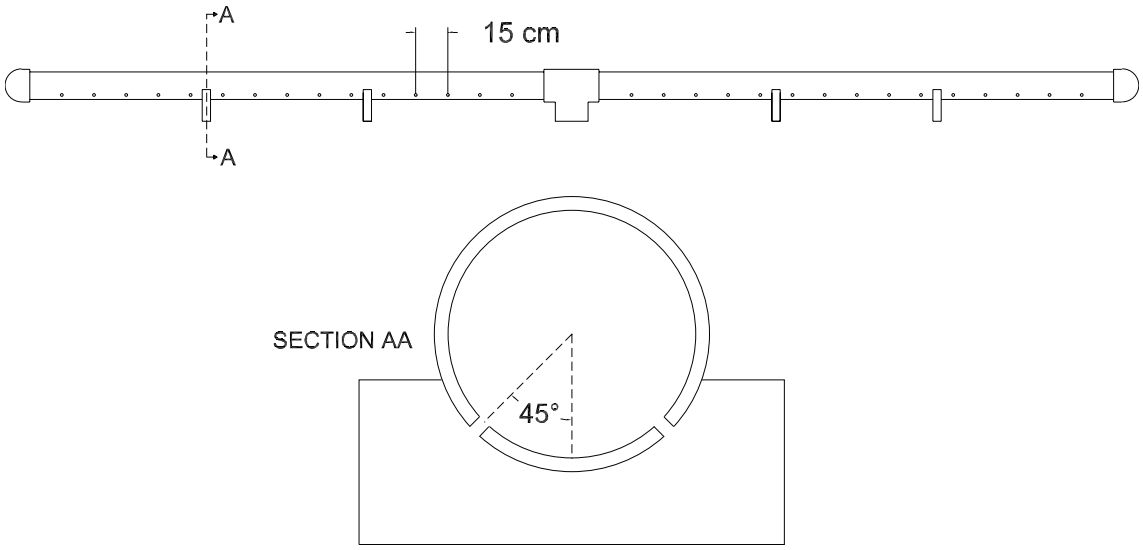

Figure 4.2: Schematic diagram of the line diffuser and its cross-section used to create a laminar jet for stratifying the tank.

4.1.1 Internal Wave Apparatus

The internal wave apparatus consisted of several components attached to the main tank (Figure 4.3). Following the theory described in Dean and Dalrymple [1991], a half-cylinder plunger-type wavemaker was made to create a perturbation in the pycnocline represented by the interface between the density layers.

The wavemaker plunger was made out of Type 2 PVC and had dimensions of 10.16 *cm* diameter and 50 *cm* length. Detailed schematics of the wavemaker components are shown in Figure 4.5. The wavemaker was driven by an electric motor (Dayton DC Gearmotor Model 4Z728A). A careful calibration was performed to relate the control voltage to the speed of rotation (Figure 4.4). A power-function trend line shows the relationship between the voltage (y) and the time per revolution of the disk (x) to be given as $y = 2.6953x^{-0.547}$ with a R^2 value of 0.979. A DC power supply (HP 6205C Dual DC Power Supply) provided the control voltage for the motor controller,

and the control voltage was quantified with a digital multimeter. Figure 4.5a shows the stainless steel linkage used to connect the plunger to a disk connected to the rotating motor shaft. The linkage had a thickness of 0.635 *cm*, length of 42.5 *cm*, and width of 2.54 *cm*. The disk, made out of aluminum, is shown in Figure 4.5b with an outer diameter of 17.8 *cm*. Figure 4.5c shows an aluminum switch-striking tab. The holes on the three elements all had a diameter of 7.94 *mm* and were connected using shoulder bolts. The hole located on the bottom of the linkage was used to connect to the plunger, and the upper three holes (labeled $\#1-3$) are used to connect to one of the inner four holes (labeled $\#5-8$) on the disk. Different combinations of hole connections allowed flexibility in adjusting the resting position of the plunger and the amplitude of the plunger motion. The height of the plunger at its resting position must match the height of the interface, which corresponded to the thickness of the bottom layer (h_1). The inner holes on the disk provided a range of amplitudes from 3 *cm* to 6 *cm*. The outer holes on the disk ($\#1-4$) were each 7.5 *cm* from the center of the disk and were used to attached the switch-striking tab to the disk.

The switch-striking tab was bolted to the outer hole that radially aligns with the location of the connection to the linkage to the plunger. The switch-striking tab tripped the switch button, mounted directly above the disk. On each revolution the switch sent a voltage signal (generated with HP 6205 C Dual DC Power Supply) to the external trigger port of a pulse generator (Berkeley Nucleonics Corp. [BNC] Model 500). By precisely controlling the delay following the external trigger signal, the pulse generator sent a signal to the camera to capture an image at a targeted phase of the standing wave cycle.

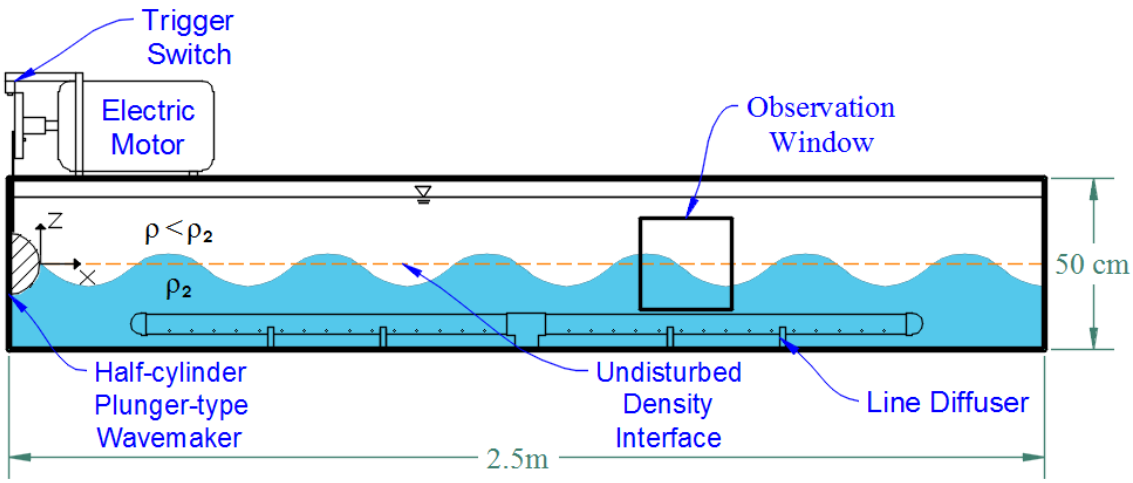

Figure 4.3: Schematic diagram of the internal wavemaker apparatus.

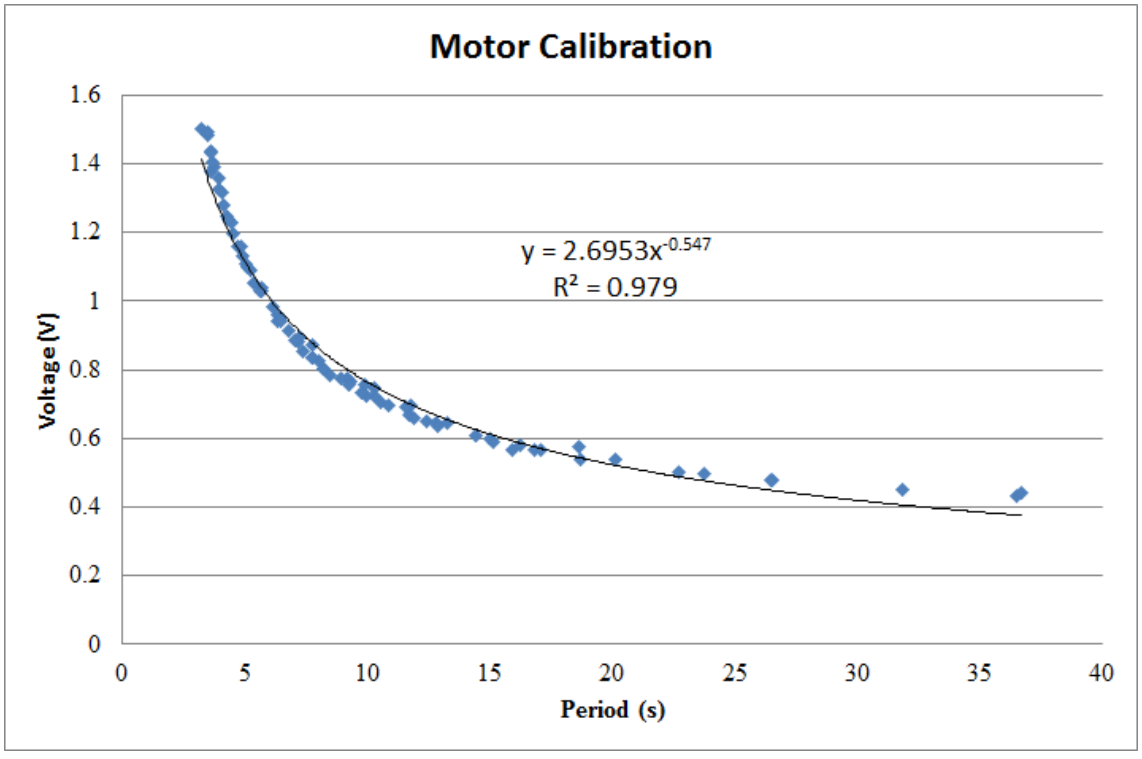

Figure 4.4: A calibration curve for the gearmotor showing the variations of voltage as a function of time per revolution of the disk.

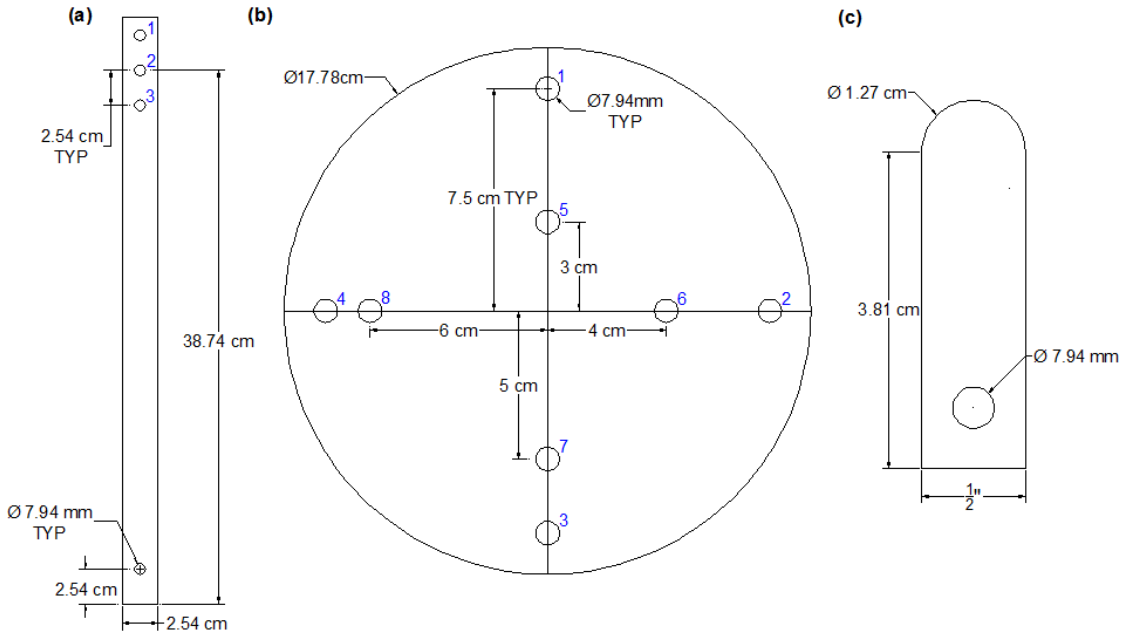

Figure 4.5: Sketch of the wavemaker components. (a) Stainless steel linkage. Holes $\#1-3$ were used to adjust the plunger height to match the thickness of the layer. (b) Aluminum disk that connects the stainless steel linkage to the electric motor shaft. Holes $\#1-4$ were used to connect the switch-striking tab, and holes $\#5-8$ were used to adjust the amplitude of the generated internal wave. (c) Aluminum switch-striking tab that was bolted to the aluminum disk and struck the trigger switch once per rotation.

4.1.2 Experimental Parameters

The design parameters for a standing internal wave were chosen in order to mimic the thin layer structures found in highly stratified coastal environments (Cheriton et al. 2009; Velo-Suarez et al. 2010). In determining the parameters, several constraints were taken into account such as the tank dimensions, the size of the wave with respect to the observation window, and the resolution of the recorded images.

To test the apparatus, three cases were chosen based on the analytical solution of the standing internal wave in a two-layer stratification system. Table 4.1 summarizes the different wave parameters for each case. The independent variables were: (1) the fluid density jump between the layers, (2) the amplitude of the wave, (3) the layer thickness, and (4) the seiching mode of the wave. The wave period was calculated from these input variables. Based on the solution (Equation 3.43) obtained by solving the boundary value problem for a two-layer system that satisfied the kinematic surface, dynamic surface, kinematic interface, and the dynamic interface boundary conditions, there were two roots of the equation. This indicated two possible modes for layers 1 and 2 (h_1 and h_2): positive and negative modes. The 'positive' mode (the quadratic solution from adding the square-root term to the $-b$ term) was the higher-order solution that could be neglected, and the 'negative' mode was the term of physical interest. The wave period was then determined based on the calculated circular frequency (of the 'negative' mode).

The density jumps of 0.75, 1.0, and 1.5 σ_t units were chosen based on previous copepod behavior assays performed by Woodson et al. (2007a). This study showed that based on a regression analysis of the number of individual calanoid copepods (*Temora longicornis* and *Acartia tonsa*) crossing versus the magnitude of the density jump, the threshold boundary range was between $\Delta\sigma_t = 0.4$ to 2.0. The lower boundary was where the regression curve began to decrease, and the upper boundary was where approximately 75% of the population was not crossing. The amplitude of

the plunger was experimentally determined to be 3 cm; anything greater produced a nonlinear internal wave and eventually started breaking. At larger amplitudes, higher harmonics and evanescent modes were also generated. Based on the theoretical considerations, the layer thicknesses must be equal (i.e., $h_1 = h_2$), and the thickness was arbitrary as long as it was significantly greater than the amplitude. A limiting factor in the layer thickness for this apparatus was that the linkage (Figure 4.5a) had only three height settings; however, this can be modified easily for future studies by fabricating a linkage with different length and hole positions.

The seiching mode number was equal to the harmonic mode of a standing wave, which dictated the number of full wavelengths in the tank. The mode was determined by two main criteria: (1) to capture at least a quarter wavelength in a 30 $cm \times 30$ cm viewing window in order to uniquely pinpoint any location on the wave at a given time and to maintain enough imaging resolution to resolve the wave interface position, and (2) to lower the wave period by increasing the mode due to viscosity becoming dominant at periods above ~ 27 seconds at an amplitude of 3 cm.

Table 4.1: Parameter specification for the three experimental cases. The table includes fluid density jump, amplitude of the plunger motion, layer thickness, seiching mode number, and wave period.

Case Number	**Density Jump at 12 °C** ($\Delta\sigma_t$)	**Amplitude** (cm)	**Layer Thickness** $h_1 = h_2$ (cm)	**Seiching Mode Number**	**Wave Period** (s)
1	0.75	3	22.2	16	23.1
2	1.0	3	22.2	12	23.5
3	1.5	3	22.2	8	23.4

4.1.3 Stratification Techniques

A two-layer stratified volume was prepared prior to running both the flow characterization and behavior assay experiments. All components were thoroughly cleaned with disinfectant solution to remove any contaminants in the system since live animals were being used. The fluid for the density layers were created in separate batches using filtered artificial seawater (Instant Ocean). The lighter density layer (ρ_1, referred to as the 'upper layer') was prepared in the experimental tank with a salinity of 33 ppt. The heavier density layer (ρ_2, the 'lower layer') was prepared in the reservoirs with a salinity of 33.75 ppt for case 1, 34 ppt for case 2, and 34.5 ppt for case 3. The salinity levels were chosen to best match natural levels in the ocean where the copepods were harvested. To avoid damaging the acrylic tank a submersible pump was used for mixing the upper layer fluid, and an industrial mixer (Neptune Mixer Co.) was used for mixing the fluid in the reservoir. The seawater solutions were mixed over a period of two days to allow the mixture to settle overnight in order to ensure homogeneous mixing. Before stratifying the volume, the wavemaker plunger was positioned at the desired height. This step was crucial because once the tank was stratified, moving the wavemaker plunger would disturb the interface. For visual characterization, red food coloring (Klecknes's Tomato Shade Food Coloring) was mixed into the bottom layer fluid. The lower layer was slowly introduced to the tank via the line diffuser at the bottom of the tank. The flow rate was initially 1.9 *L/min* until the depth of the incoming layer was greater than the height of the diffuser. Then the flow was increased to 7.6 *L/min*. The incoming flow rate was specified to maintain laminar flow in the jet flows exiting the diffuser holes in order to avoid turbulent mixing. The flow regime (laminar or turbulent) is determined by the Reynolds number, Re:

$$Re = \frac{uD}{\nu} \tag{4.1}$$

where u is the individual diffuser jet velocity, D is the diameter of the diffuser holes,

and ν is the kinematic viscosity of saltwater. By using the continuity equation and assuming 60 holes (n) on the line diffuser, the minimum diameter to maintain a laminar jet flow was calculated. The Reynolds number at which a flow transitions from laminar to turbulent is 2000 [Fischer et al. 1979].

$$Re = \frac{4Q}{n\pi D\nu} \tag{4.2}$$

$$D = \frac{4Q}{n\pi\nu Re} \tag{4.3}$$

For flow rate (Q) of 1.9 L/min, Equation 4.3 yielded a minimum diameter of 0.258 mm thus our chosen diffuser hole diameter of 2.54 mm was well within the laminar flow regime (i.e., corresponds to $Re = 210$). The layer structure was assumed to be steady over the course of the experiments ($\sim$ 2 hours) because of the long time scales ($\sim$ days) associated with molecular diffusion.

4.2 Flow Characterization Techniques

A standing internal wave was created by moving the wavemaker plunger at the targeted frequency and amplitude to perturb the pycnocline. For the wave characterization trials, the layers were marked by the sharp interface between the red bottom layer and clear upper layer. After initiating the wavemaker motion, the waves took about 30 minutes (on average) to develop into a standing wave due to the long wave period and return time of the reflected waves.

4.2.1 Components and Data Capture

A CCD camera (Vision Research Inc. model Phantom v210) with 60 mm focal length lens (Nikon) was used to record the interface location. The resolution of the

camera was 1280 × 800 pixels, but only 800 × 800 pixels were used due to the square observation window shape. The images a spatial resolution of 0.375 mm/pixel , which provided high resolution of the internal wave interface location. The exposure was set to 750 μs and f-stop to f/2.8 to get the necessary depth of field and attaining sufficient brightness for the imaging. The camera was mounted on a tripod at a distance of 0.8 m from the front wall of the tank. To illuminate the tank and the flow field, 5 lamps using fluorescent coil bulbs were used. As shown in Figure 4.6, three lamps were positioned at 45° facing downward toward the back wall of the tank and one lamp was positioned on each end, angled inwards towards the observation region. A piece of white paper was used to diffuse the light from the lamps on the sides. A white plastic sheet was attached to the back of the tank to create a background that enhanced the sharp color contrast between the two layers.

Two different triggering strategies were required for capturing still images for (1) flow visualization, and (2) recording an image sequence for signal processing. First to capture still images, the triggered pulse generator was used to control the image acquisition with a precise delay to capture an image at the targeted phase in the cycle (as described above). Images were captured for eight phases in the cycle for flow visualization purposes.

The camera setup for recording image sequences for signal processing required throttling the frame rate of the camera. In this arrangement, the trigger signal was not phase-locked with the wavemaker motion. The minimum frame rate of the Phantom camera was 24 fps, but the objective was to record at a slower rate in order to increase the total duration of the image sequence and achieve a higher resolution estimate of the dominant frequency during signal processing. The frame rate was lowered to 4 fps by using the camera's trigger mode option and sending a trigger signal for each frame capture. Three sequence of 7200 images was captured in this manner for each case.

Figure 4.6: Photograph of the apparatus showing the lighting arrangement during flow visualization.

4.2.2 Data Processing

The generated wave frequencies in the time record of wave height were quantified using signal processing. First, the recorded videos were calibrated for distortion via the camera control software (i.e., Vision Research Phantom Camera Control Application). This file was exported as an '.avi' file and imported into MATLAB (The MathWorks, Inc., Natick, MA) for post-processing. Next, a time stack image at an anti-node of the wave was created via MATLAB. Two image processing filters, median and sharpen, were used to reduce the noise and sharpen the image in order to use the *Sobel* method edge detection algorithm, which reliably identified the interface location (and hence the wave height).

A fast Fourier transform (FFT) algorithm was used to convert the extracted time record of wave height to the frequency domain. For the cases presented in this thesis, a single dominant frequency appeared. If multiple large-peaks were observed, then energy exchange between frequencies or beating of the signal must be considered. To avoid generating higher harmonics, the wave must be linearized by decreasing the amplitude of the wave.

4.3 Behavioral Assays and Data Analysis Techniques

For the behavioral assays, a mixed population of three species of copepods was used: *Acartia tonsa*, *Temora longicornis*, and *Eurytemora affinis*. The main goal of this study was to observe the animals' behavioral response to the fluid density stratification and internal wave.

4.3.1 Copepod Collection and Maintenance

The copepod specimens were collected on August 15, 2015 in the harbor of Boothbay, ME, USA (Latitude: 43.860 N, Longitude: 69.582 W). The copepods were collected by Dr. David Fields of Bigelow Laboratory for Ocean Sciences. The tow was done during the hours of 12:00 - 12:30 pm using a 153 micron net. The deployment was a surface tow during high tide for 30 minutes off of the Bigelow dock. The animals were contained in eight $1 - L$ bottles with food (Rhodomonas) and shipped overnight to the Georgia Institute of Technology (Atlanta, GA) in a cardboard box with a Styrofoam cooler.

Once the shipments arrived at the Georgia Institute of Technology, the mixed population of copepods were placed into two five gallon buckets for culture in the temperature controlled environmental room of Dr. Jeannette Yen (School of Biology). The culture media was made up of artificial seawater (Instant Ocean) at salinity level of 33 ppt, and the ambient temperature was kept at 12°C in order to match natural environment conditions. Copepods were fed both Isochrysis and Tetraselmis spp. phytoplankton every other day.

4.3.2 Behavioral Assays

Behavioral assays were conducted in the same internal wave apparatus as the flow characterization experiments (Figure 4.3). All experiments were conducted at constant temperature (12 ± 0.2 °C). In each trial, 200 fresh copepods of mixed population were used. The behavioral assays were performed with artificial seawater (Instant Ocean). A $30\ cm \times 30\ cm$ window was used to observe the copepod swimming kinematics. The observation window was positioned such that the undisturbed density interface (h_1) was at the mid-line.

Two 7-W continuous-wave infrared laser (CrystaLaser, Inc.) with a wavelength of $808\ nm$ were used. The lasers were mounted behind the tank at 45° angles and diffused

via 50° circular, top hat diffusers (Thorlabs model ED1-C50-MD) to provide sufficient illumination in the observation region (Figure 4.1). Infrared (IR) lighting was chosen because copepods typically cannot sense light at this wavelength; therefore, their swimming behavior was not modified during the observation. The Phantom v210 camera was used with a 60 mm focal length lens (Nikon). The exposure time was set to 2400 μs and the camera was positioned 0.77 m away from the front wall of the tank. The spatial resolution of the recordings was 0.394 mm/pixel. The frame rate was 15 fps because it provided sufficient temporal resolution to accurately quantify swimming behaviors.

The behavior assays were conducted for three different physical arrangements: (1) stagnant fluid with no density stratification (i.e., Control), (2) stagnant two-layer density stratification, and (3) two-layer density stratification with standing internal wave motion. Table 4.2 shows the parameters for each case. Behavioral trials were conducted for one case of wave parameters (case 2 from Table 4.1).

Five 5-minute bursts of image sequences were recorded. The trajectories were manually tracked in DLTdv5, a MATLAB particle tracking software developed by Hedrick (2008). Because the recordings were triggered by the trigger-switch (at the initiation of the image sequence acquisition), we were able to superimpose the theoretical standing wave with matching wave conditions to the digital recordings at 15 fps. The time-resolved 2-D quantification was used to calculate the average of the absolute vertical distance between the copepod position and the wave interface. Additionally, the paths of neutrally buoyant particles were calculated using a Lagrangian velocity (assume Eulerian velocity $\sim$ Lagrangian velocity since the displacement is small) to compare with the experimental trajectories.

Table 4.2: Experimental parameters for the behavioral assays.

Case	**Stratification?**	**Wave?**	**f-stop**	S_1 **(ppt)**	S_2 **(ppt)**	**Period (s)**
Control	No	No	f/11	33	N/A	N/A
Stagnant Density Jump Treatment	Yes	No	f/11	33	34	N/A
Internal Wave Treatment	Yes	Yes	f/8	33	34	23.46

CHAPTER V

RESULTS AND DISCUSSION

5.1 Flow Characterization

This section characterizes the standing internal wave flow for three cases in a two-layer stratification system. The wave parameters (Table 4.1) were chosen based on previous observations of copepod behavior (Chapter 2) and theoretical calculations of the internal wave flow (Chapter 3). The results of the flow characterization by flow visualization and signal processing are presented here.

5.1.1 Case 1: $\Delta\rho = 0.75\ \sigma_t$

Case 1 had a density jump of 0.75 σ_t, piston-displacement amplitude of 3 *cm*, wave period of 23.11 seconds, and seiching mode of 16. Figure 5.1 shows the flow visualization of a complete wave cycle at eight equally-spaced phases. The interface shows a partial standing wave (nodes and antinodes indicated on the figure) with some nonlinear waves being generated.

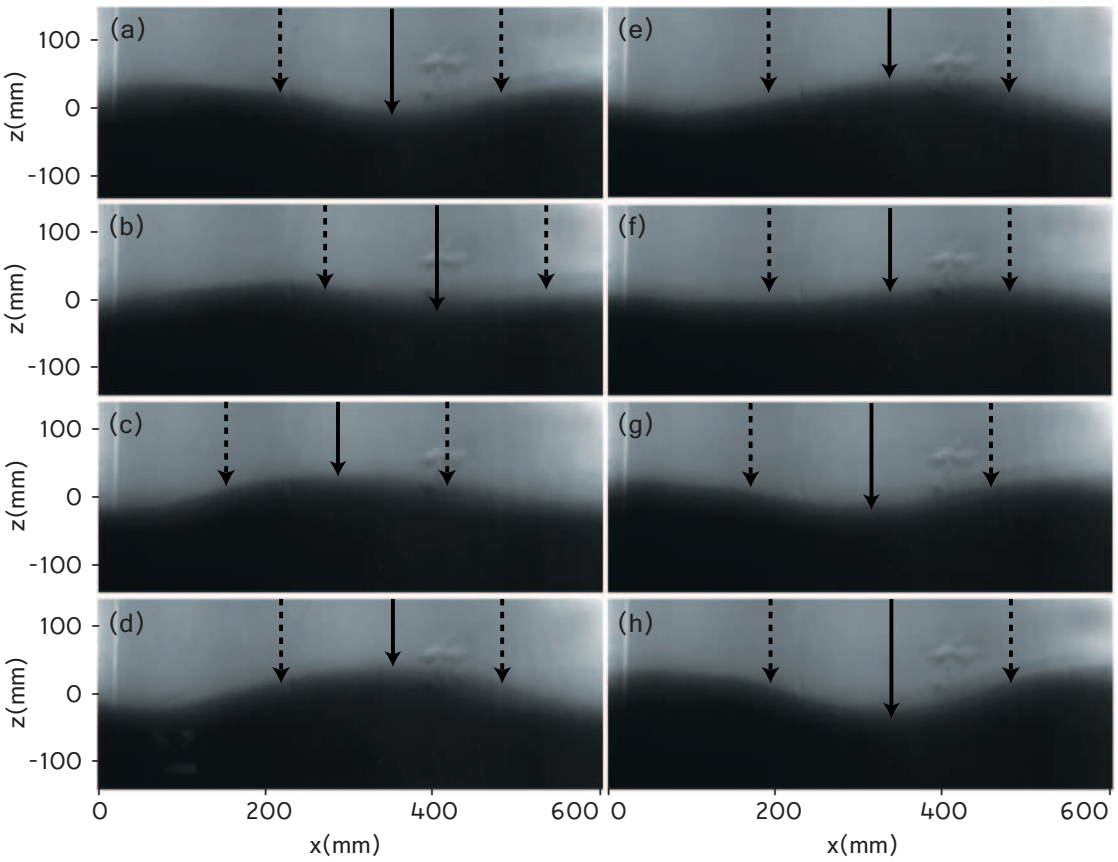

Figure 5.1: Flow visualization for Case 1 showing eight phases $(a - h)$ of a full wave cycle. The phases correspond to $\phi = 0$, $\frac{\pi}{4}$, $\frac{\pi}{2}$, $\frac{3\pi}{4}$, π, $\frac{5\pi}{4}$, $\frac{3\pi}{2}$, and $\frac{7\pi}{4}$ [radians] respectively. The locations of the nodes are marked by the vertical dotted arrows and the antinodes by the solid arrows.

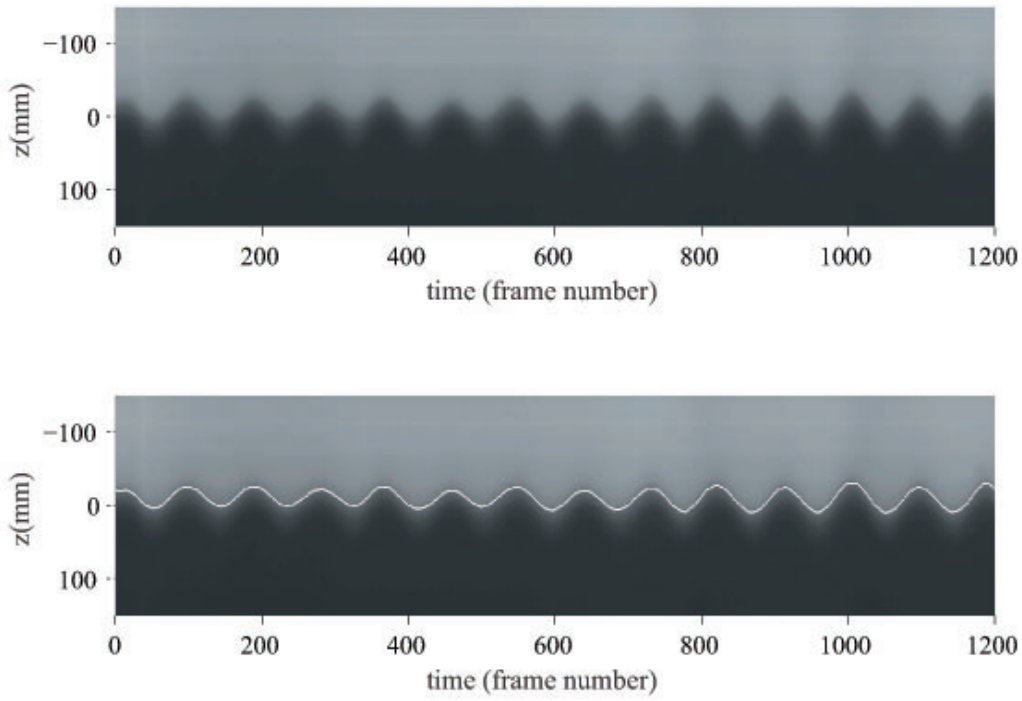

Figure 5.2: For Case 1, (a) time stack image at an antinode, and (b) the digitally-extracted interface location (white line) superimposed on the time-stack image.

The time-stack image at an arbitrary location of the standing wave is shown in Figure 5.2a. The time stack image is created by extracting a vertical line of pixels from the identical horizontal location (selected to match an antinode location) in each image of the recorded sequence and re-arranging them side-by-side to effectively form a time series at that horizontal location. The image shows non-constant wave heights indicating possible mixing at the interface and possible generation of non-linear waves that would cause higher harmonic modes to be created. Figure 5.2b shows the digitally detected interface (white line) superimposed on the time-stack image. The detected interface accurately captured the oscillation of the interface including the non-constant wave heights observed in the time-stack image.

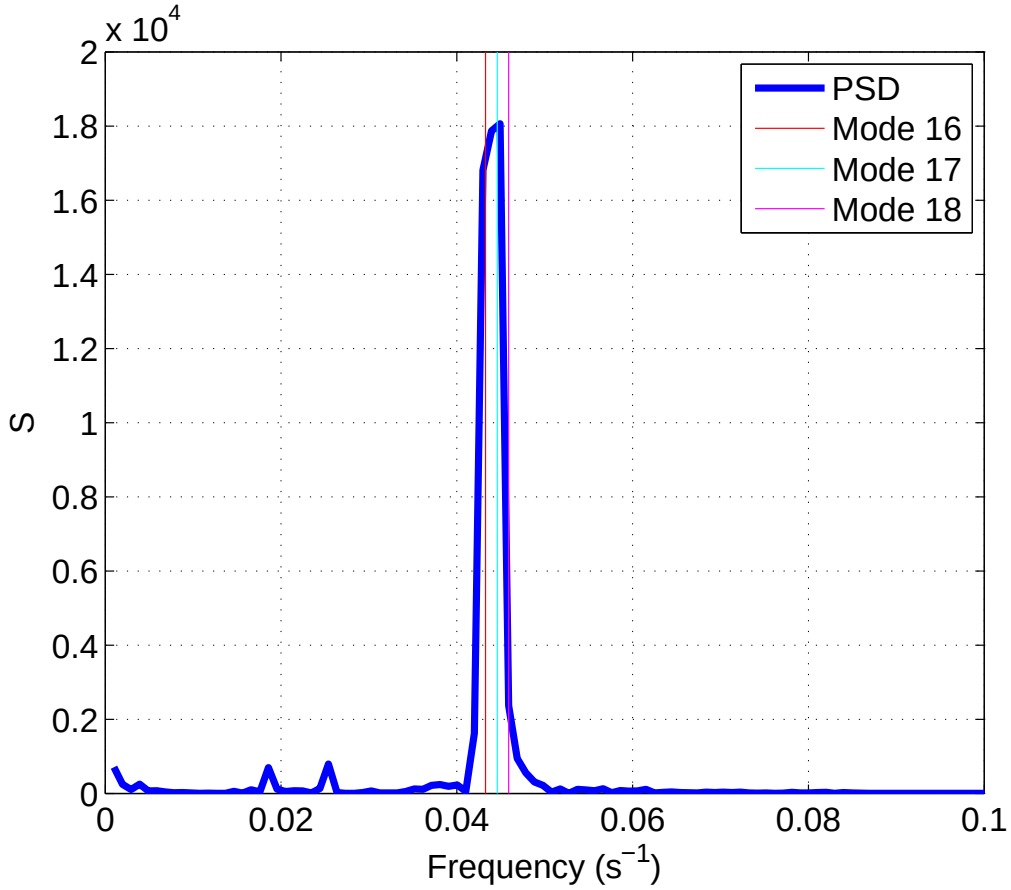

Figure 5.3: For Case 1, power spectral density (PSD) of the time record of the interface location shown as function of frequency. In addition, the frequencies corresponding to three modes are indicated with the vertical lines.

The power spectral density (PSD) in Figure 5.3 shows the strength of the wave signal in the frequency domain. The PSD shows a strong peak in a narrow frequency band. The band of peak frequencies corresponded to mode numbers ranged between 16 and 18, with the target mode as 16. The multi-mode coverage of the peak frequency agrees with the irregular wave heights seen in the time-stack images.

5.1.2 Case 2: $\Delta\rho = 1.0\ \sigma_t$

Case 2 had a density jump of 1.0 σ_t, piston-displacement amplitude of 3 *cm*, wave period of 23.46 seconds, and seiching mode of 12. Figure 5.4 shows the flow visualization of the interface at eight phases. The flow visualization shows a clear standing wave with the nodes and antinodes.

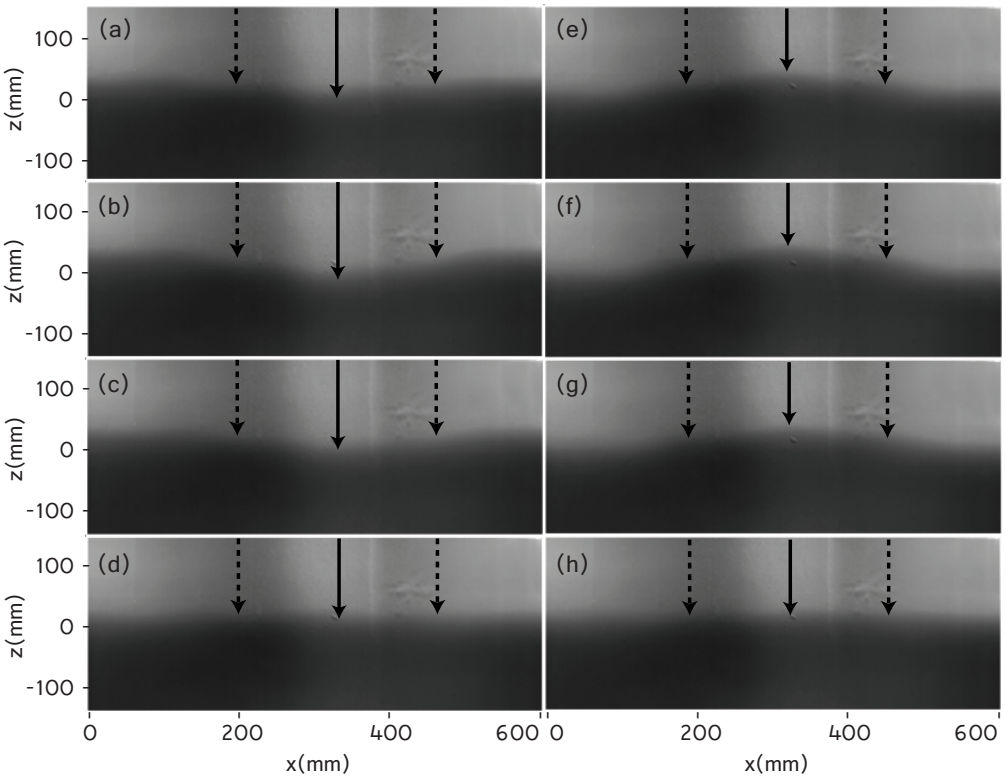

Figure 5.4: Flow visualization for Case 2 showing eight phases $(a - h)$ of a full wave cycle. The phases correspond to $\phi = 0$, $\frac{\pi}{4}$, $\frac{\pi}{2}$, $\frac{3\pi}{4}$, π, $\frac{5\pi}{4}$, $\frac{3\pi}{2}$, and $\frac{7\pi}{4}$ [radians] respectively. The locations of the nodes are marked by the vertical dotted arrows and the antinodes by the solid arrows.

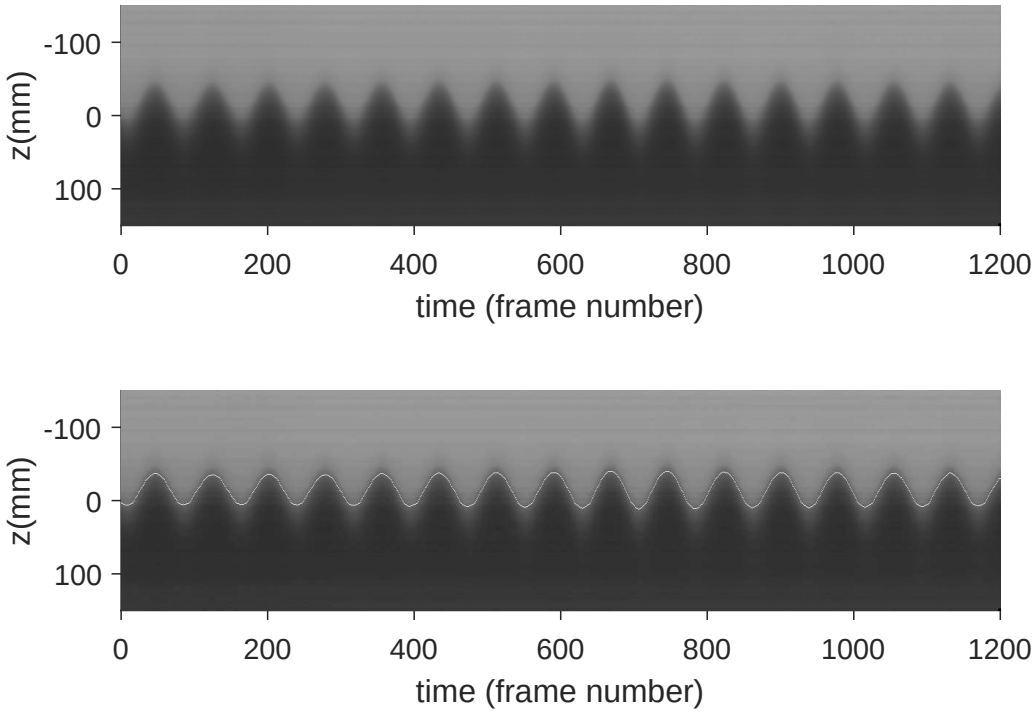

Figure 5.5: For Case 2, (a) time stack image at an antinode, and (b) the digitally-extracted interface location (white line) superimposed on the time-stack image.

The time-stack images at the antinode of the standing internal wave is shown in Figure 5.5. The wave heights in the time-stack (Figure 5.5a) are shown to be highly regular and consistent. Figure 5.5(b) shows the digitally detected interface superimposed on the time-stack image. The white line accurately captures the oscillating interface and further supports the previous observation that the wave heights are regular as a function of time.

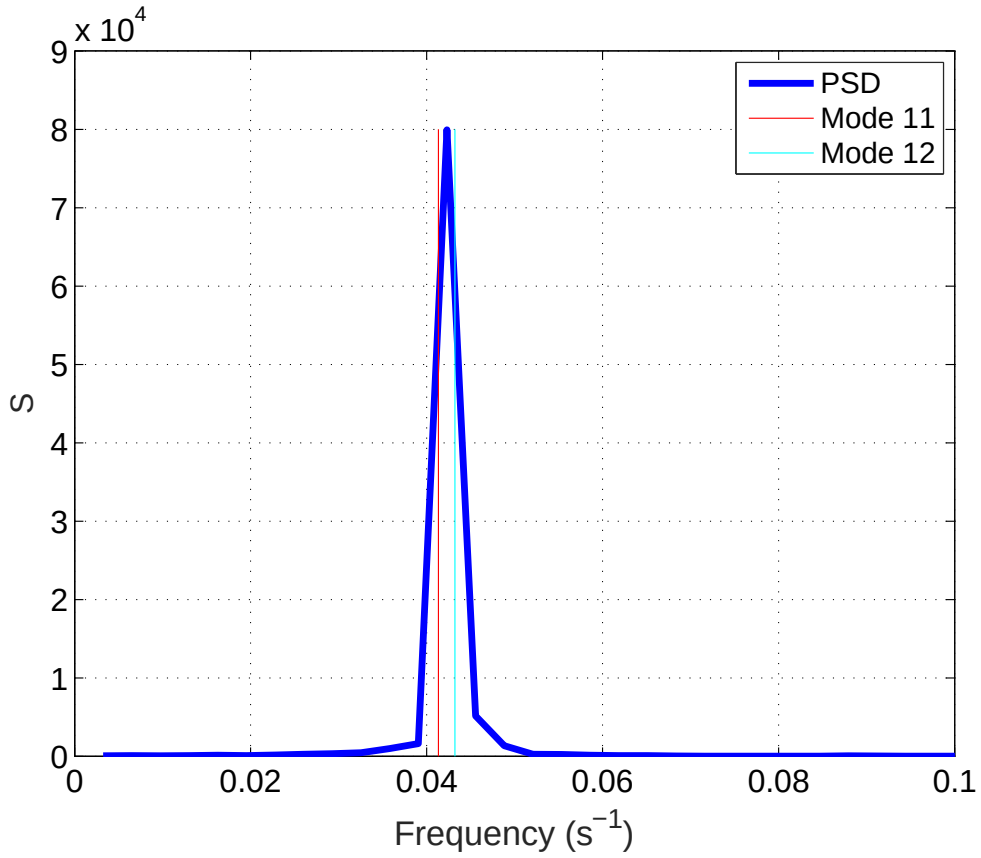

Figure 5.6: For Case 2, power spectral density (PSD) of the time record of the interface location shown as function of frequency. In addition, the frequencies corresponding to two modes are indicated with the vertical lines.

The power spectral density (PSD) (Figure 5.6) shows a narrow peak indicating that the wave is at a single harmonic mode number and no higher energy waves (non-linear waves) are being generated. The peak is between mode 11 and 12, where the target mode was 12. The peak is between two modes (as opposed to isolating a single value) because of the limited temporal resolution of our recorded image sequence. Additionally, the spectral significant wave height (H_{mo}) was calculated based on the PSD which yielded a value of 5.5 *cm*.

Figures 5.7 - 5.10 plot the theoretical velocity vectors, the iso-contours of theoretical velocity magnitude, and the theoretical shear strain rate for the first four phases

(a), (b), (c), and (d) which correspond to $\phi = 0$, $\frac{\pi}{4}$, $\frac{\pi}{2}$, and $\frac{3\pi}{4}$ respectively. Phases $e - h$ are symmetric counterparts for the phases shown. The measured amplitude (calculated from H_{mo}) was used in calculating the theoretical flow fields. The velocities are maximum at the interface ($z = -h_1 = -0.22\ m$) and decay away from it. The iso-contour plot shows the maximum velocity to be at the interface as well with a peak value of $0.015\ m\ s^{-1}$. The shear strain rate plot shows the maximum value to be at the interface with a peak value of $0.044\ s^{-1}$. The velocities and the strain rates are at minimum (nearly zero) for phases $(a)\ \phi = 0$ and $(e)\ \phi = \pi$ and at maximum for phases $(c)\ \phi = \pi/2$ and $(g)\ \phi = 3\pi/2$.

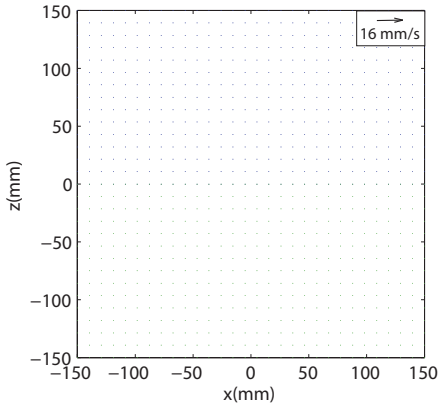

(a) Velocity Vectors

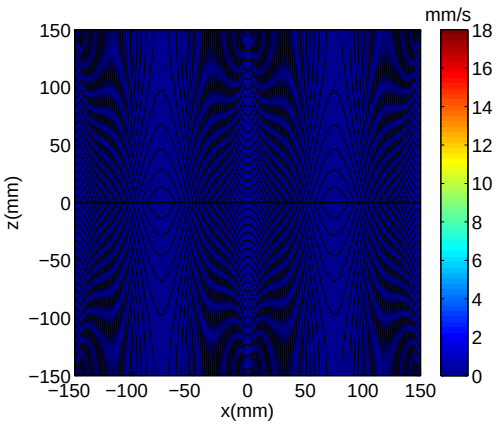

(b) Velocity Magnitude [$mm\ s^{-1}$]

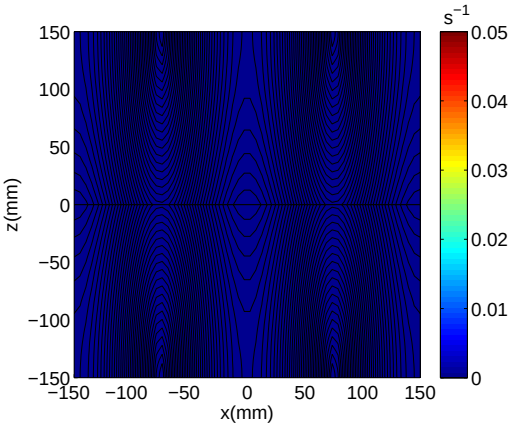

(c) Shear Strain Rate [s^{-1}]

Figure 5.7: Theoretical velocity and shear strain rate field showing the direction and magnitude at Phase a across the observation window domain. For the velocity vector plot, the upper layer is represented by the blue arrows and the lower layer is represented by the green arrows.

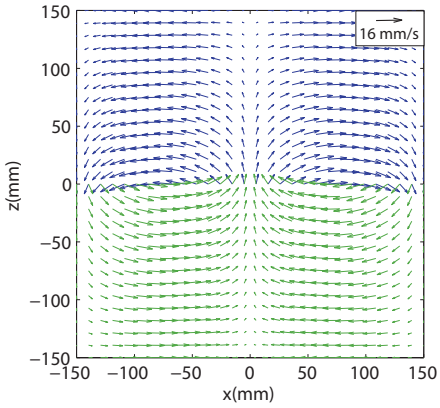

(a) Velocity Vectors

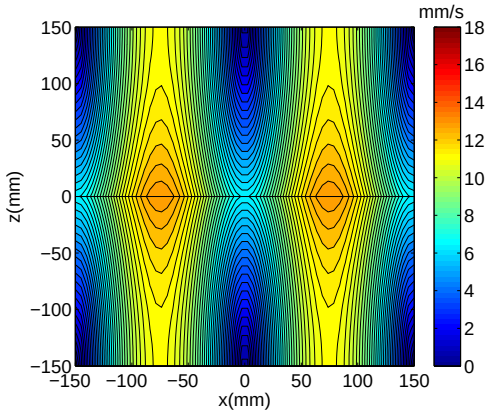

(b) Velocity Magnitude [$mm\ s^{-1}$]

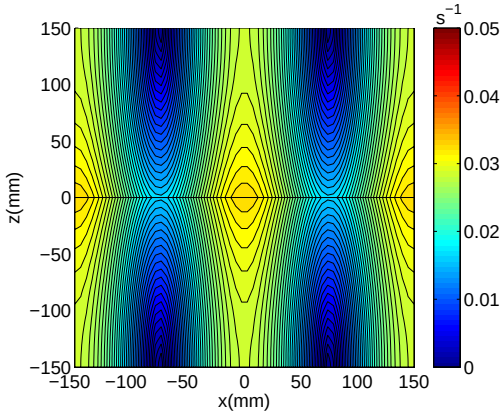

(c) Shear Strain Rate [s^{-1}]

Figure 5.8: Theoretical velocity and shear strain rate field showing the direction and magnitude at Phase b across the observation window domain. For the velocity vector plot, the upper layer is represented by the blue arrows and the lower layer is represented by the green arrows.

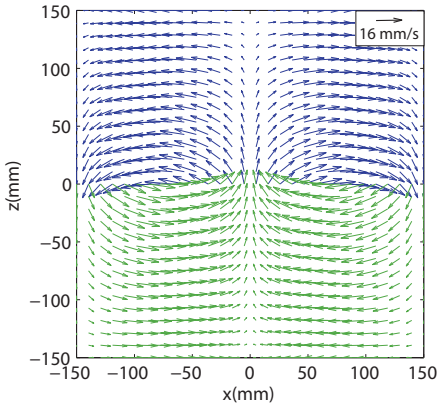

(a) Velocity Vectors

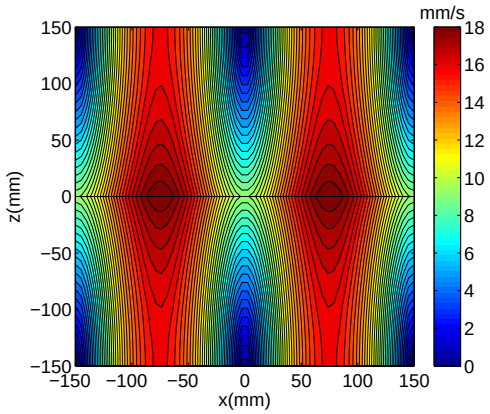

(b) Velocity Magnitude [$mm\ s^{-1}$]

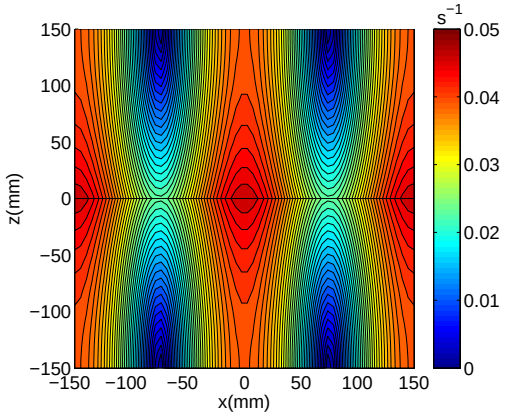

(c) Shear Strain Rate [s^{-1}]

Figure 5.9: Theoretical velocity and shear strain rate field showing the direction and magnitude at Phase c across the observation window domain. For the velocity vector plot, the upper layer is represented by the blue arrows and the lower layer is represented by the green arrows.

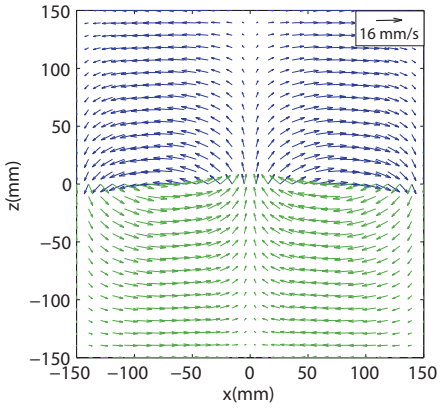

(a) Velocity Vectors

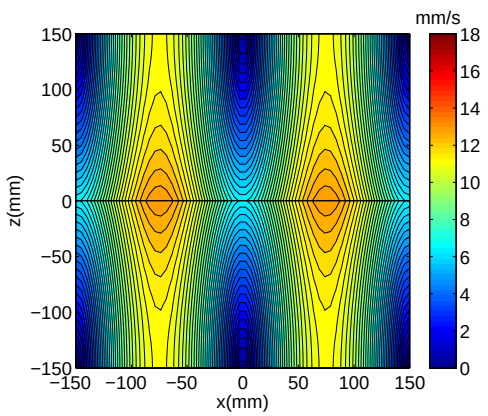

(b) Velocity Magnitude [$mm\ s^{-1}$]

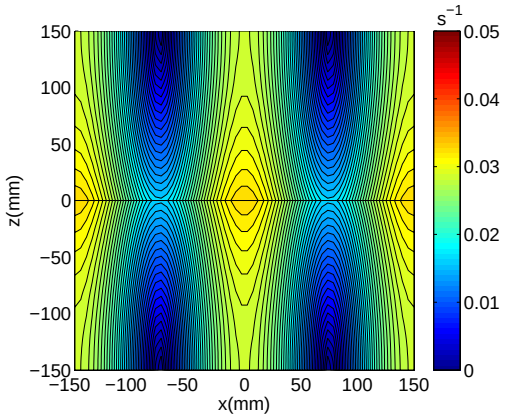

(c) Shear Strain Rate [s^{-1}]

Figure 5.10: Theoretical velocity and shear strain rate field showing the direction and magnitude at Phase d across the observation window domain. For the velocity vector plot, the upper layer is represented by the blue arrows and the lower layer is represented by the green arrows.

5.1.3 Case 3: $\Delta\rho = 1.5\ \sigma_t$

The waves properties for Case 3 were a density jump of 1.5 σ_t, piston-displacement amplitude of 3 *cm*, wave period of 23.38 seconds, and seiching mode of 8. The flow visualization images of eight phases of the wave cycle are shown in Figure 5.11.

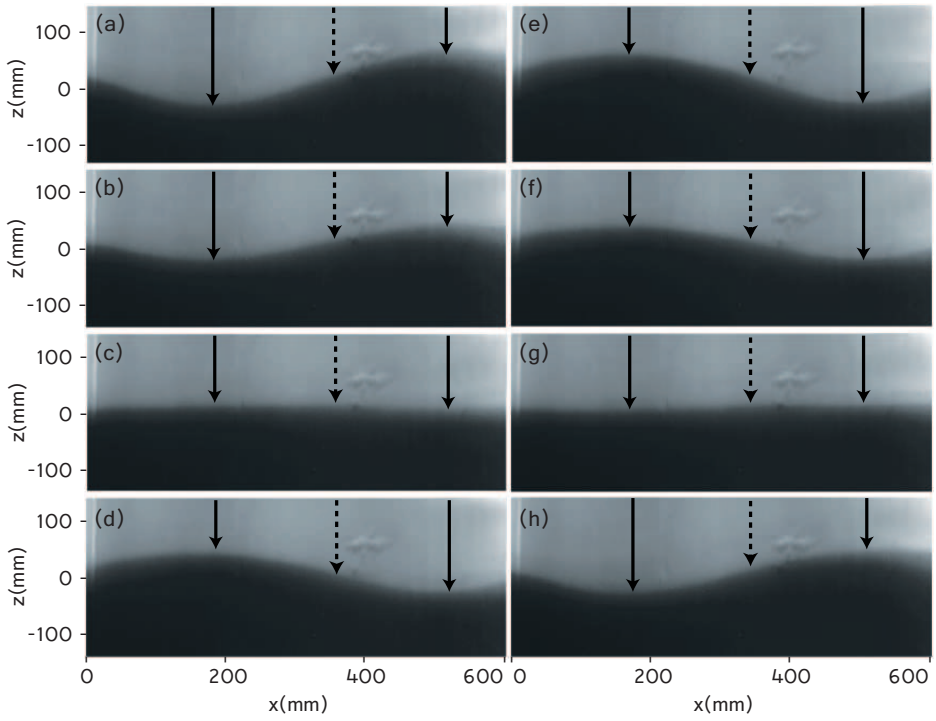

Figure 5.11: Flow visualization for Case 3 showing eight phases $(a - h)$ of a full wave cycle. The phases correspond to $\phi = 0,\ \frac{\pi}{4},\ \frac{\pi}{2},\ \frac{3\pi}{4},\ \pi,\ \frac{5\pi}{4},\ \frac{3\pi}{2}$, and $\frac{7\pi}{4}$ [radians] respectively. The location of the node is marked by the vertical dotted arrows and the antinodes by the solid arrows.

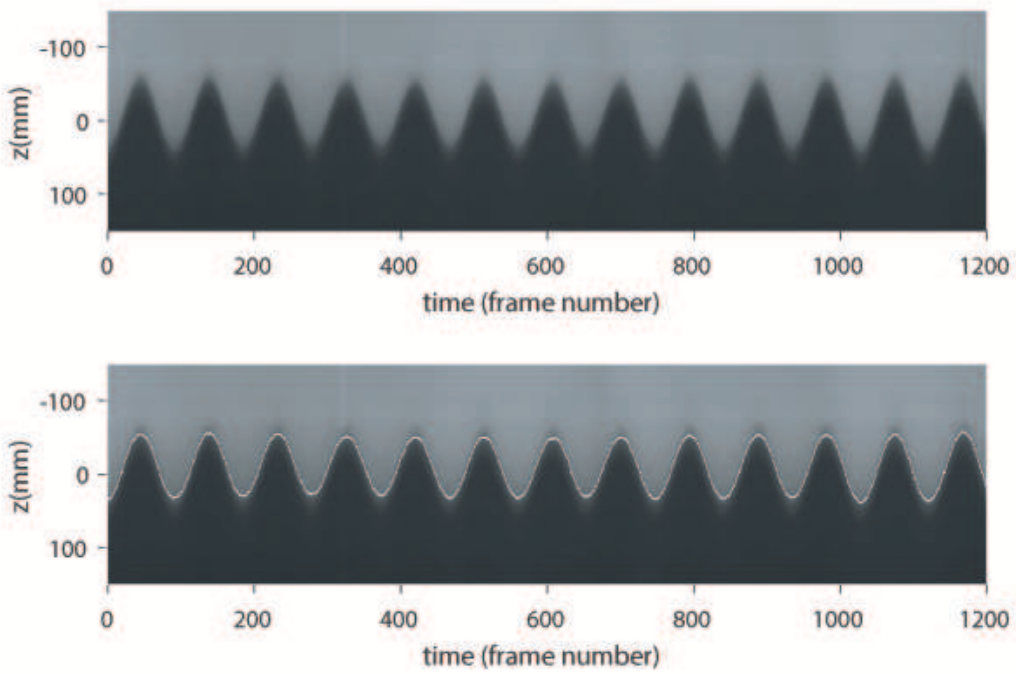

Figure 5.12: For Case 3, (a) time stack image at an antinode, and (b) the digitally-extracted interface location (white line) superimposed on the time-stack image.

The time-stack image is shown in Figure 5.12a. The image shows sharp and clear crests and troughs. The wave height is uniform and even in time. The detected interface shown in Figure 5.12b accurately captures the wave interface location. It also shows a uniform wave height across the time domain.

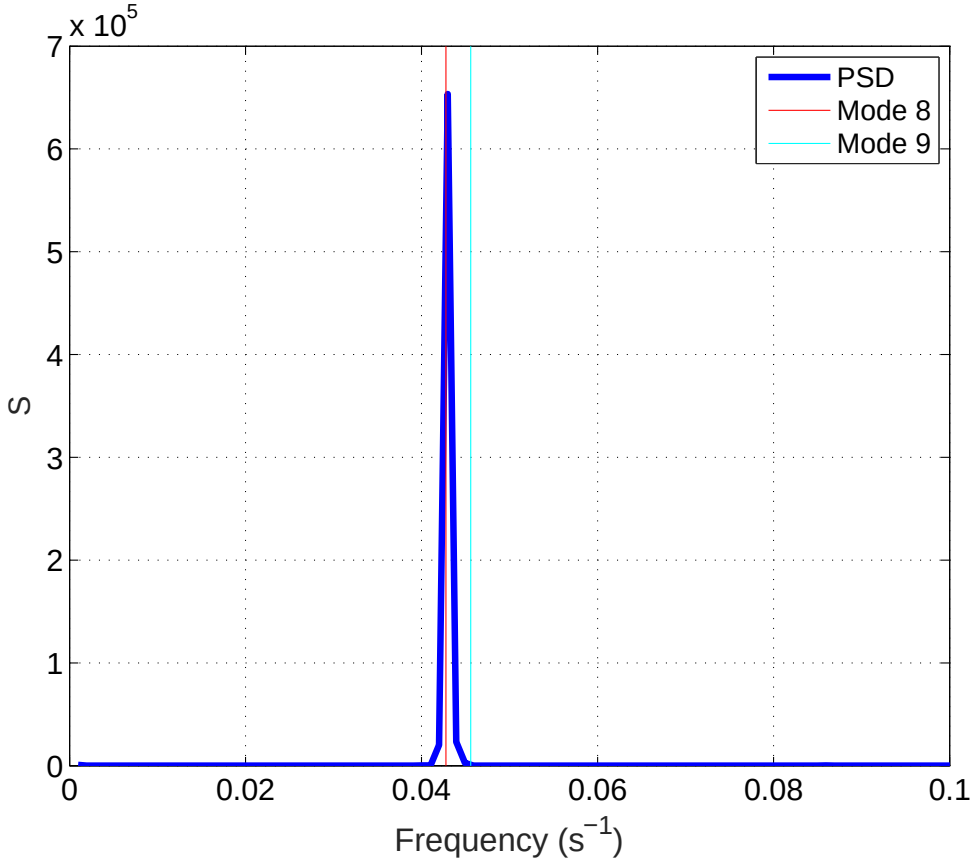

Figure 5.13: For Case 3, power spectral density (PSD) of the time record of the interface location shown as function of frequency. In addition, the frequencies corresponding to two modes are indicated with the vertical lines.

The power spectral density (PSD) shows a single dominant peak occurring at mode 8, which matched the target exactly. No other significant peaks were shown to indicate possible generation of higher energy harmonics.

5.1.4 Summary of Flow Characterization

Flow characterization results have shown that for Cases 2 and 3, the generated waves matched the targeted wave parameters almost perfectly. For both cases, the flow visualization showed a clear standing internal wave with easily identified nodes and antinodes. For both cases, the PSD of the time record of the interface location

showed a single dominant frequency being generated, which matched our target mode number.

In contrast, Case 1 was unsuccessful in creating a perfect standing internal wave. The flow visualization images show movement in the location of nodes and antinodes, and the time stack image shows that inconsistent wave heights were generated. The PSD showed a band of peak frequencies in a range around the target mode. The multi-peak frequencies may indicate non-linear waves being generated. To avoid this, the piston-displacement amplitude could be reduced to linearize the wave or the tank could be shortened. Decreasing the piston-displacement amplitude decreases the wave height and the 'ka' term (which governs nonlinear wave generation); thus ensuring the linearization of the waves. By shortening the tank, the wavelength is decreased in effect which allows for a smaller mode to be targeted.

5.2 Copepod Behavioral Assay Results

This section presents the results of the copepod swimming behavior assays. Recall from Table 4.2 that three treatments were chosen: Treatment 1 was the control case in which there was no flow and no density jump; Treatment 2 was a case with a density jump of 1.0 σ_t in stagnant water; and Treatment 3 was a case with the same density jump (i.e., $\Delta\rho = 1.0\ \sigma_t$) and an internal wave with properties matching Case 2 from the flow characterization experiments (Table 4.1).

5.2.1 Treatment 1: No Flow, No Density Jump

Figure 5.14 shows the digitized swimming trajectories for a mixed-population of copepods in a body of water with salinity of 33 *ppt*. The 25 sample tracks shown exhibited no preferential motion or swimming patterns in terms of direction. The lack

of preferential directionality in the trajectories was expected since no directionally-oriented cues (hydrodynamic or otherwise) were present in the control treatment.

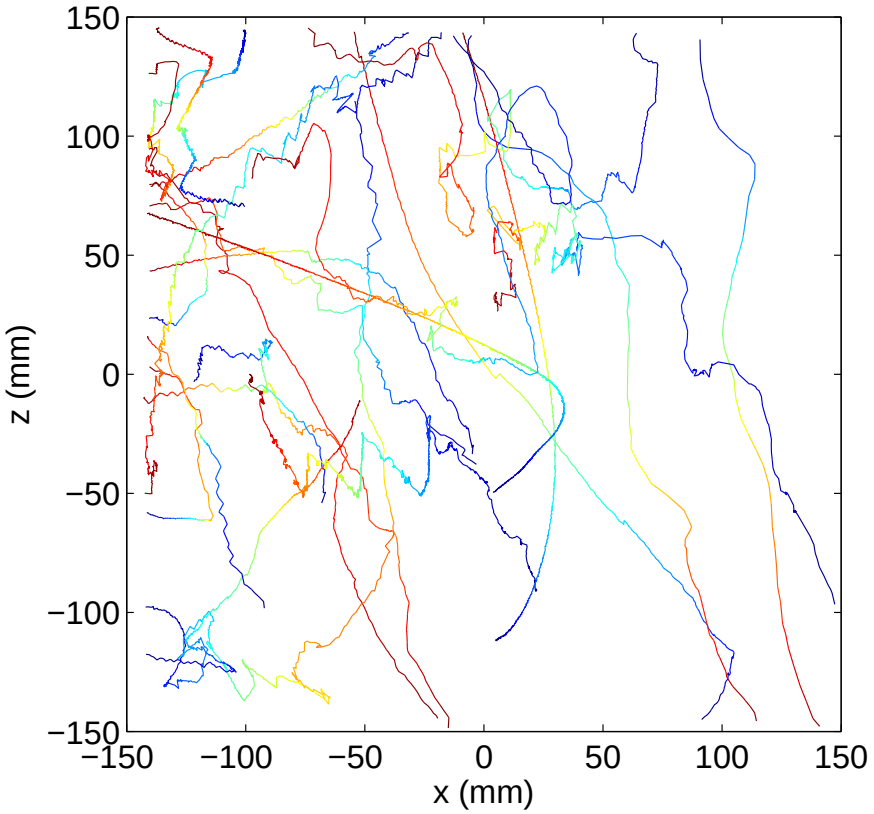

Figure 5.14: Copepod trajectories for the control treatment with no flow and no density jump. Although shown on the same plot, these trajectories were not collected simultaneously. Color indicates the passage of time with blue corresponding to the beginning of the trajectory and red corresponding to the end. A mixed population of marine copepods *Acartia tonsa*, *Temora longicornis*, and *Eurytemora affinis* were used.

5.2.2 Treatment 2: Stagnant, Density Jump

Figure 5.15 shows 25 sample trajectories for Treatment 2. The lower layer water had a salinity level of 34 *ppt* and the upper layer had 33 *ppt*. Wave motion was not introduced in this treatment. The digitized trajectories show that many of the copepods moved preferentially in the horizontal direction, parallel to the density interface. This trajectory pattern is a clear difference from Treatment 1. The apparent reluctance of some of the specimens to cross the density interface was consistent with the results for *A. tonsa* and *T. longicornis*, who for a $\Delta\rho$ of 1.0 σ_t, showed a decrease in the number of copepods crossing the density jump layer (Woodson et al. 2007a). In contrast, the other member of the tested copepod population, *E. affinis*, did not reveal a reluctance to crossing a density jump interface (Woodson et al. 2007b). The trajectories in Figure 5.15 are consistent with this reported species-specific variability in behavior with some trajectories clearly oriented parallel to the interface (and hence not crossing the interface location) and other trajectories seamlessly crossing the interface.

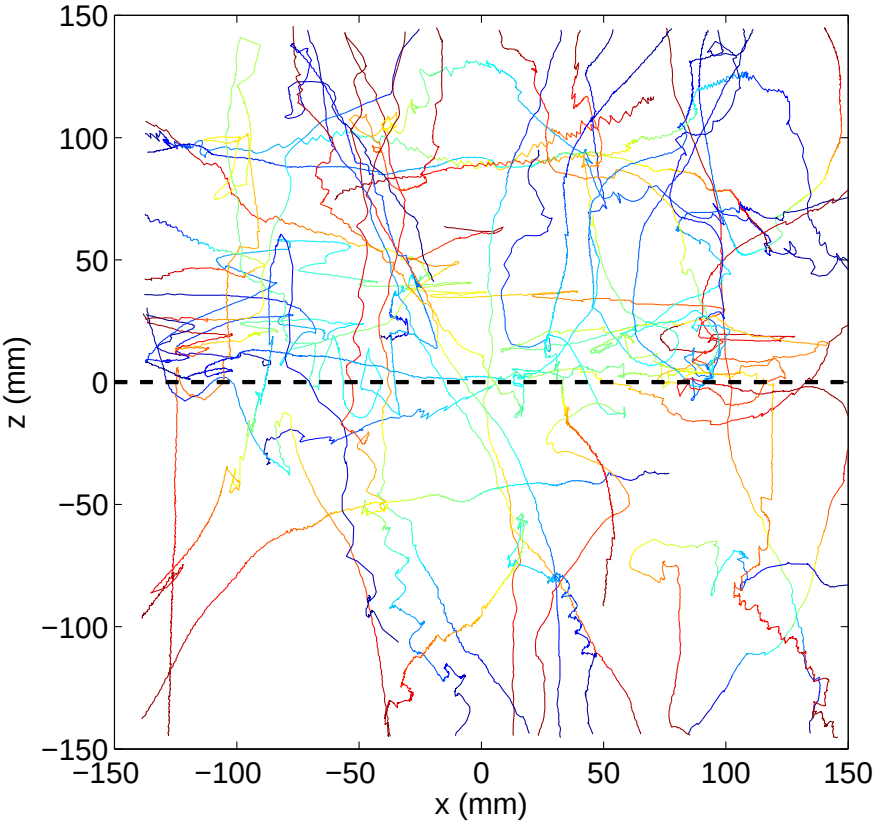

Figure 5.15: Copepod trajectories for the stagnant density jump of 1 σ_t treatment. The black dashed line indicates the location of the density interface. Although shown on the same plot, these trajectories were not collected simultaneously. Color indicates the passage of time with blue corresponding to the beginning of the trajectory and red corresponding to the end. A mixed population of marine copepods *Acartia tonsa*, *Temora longicornis*, and *Eurytemora affinis* were used.

5.2.3 Treatment 3: Internal Wave

In Treatment 3, the copepods were observed for the treatment corresponding to a standing internal wave with properties identical to Case 2 from the flow characterization experiments (lower layer salinity = 34 ppt and upper layer salinity = 33 ppt). Figure 5.16 shows 25 animal trajectories for Treatment 3. The block dotted

lines indicate the upper and lower boundaries of the internal wave as defined by the peak locations of the crests and troughs of the internal wave. The copepod swimming paths demonstrated orbital trajectories near and inside the boundaries of the internal wave. Beyond a distance of roughly 75 mm from the resting position of the interface (i.e., $z = 0$), the trajectories were much less likely to show the looping, orbital shape that is observed in the immediate vicinity of the interface location.

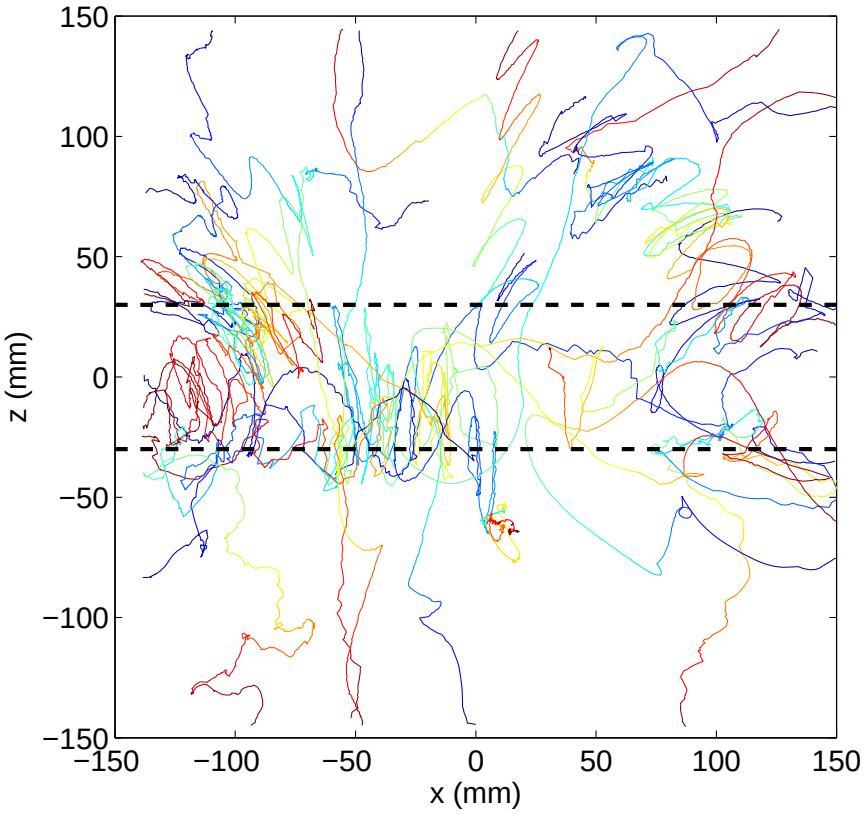

Figure 5.16: Copepod trajectories for the internal wave treatment with a density jump of 1 σ_t. The black dashed lines indicate the boundaries of the internal wave. Although shown on the same plot, these trajectories were not collected simultaneously. Color indicates the passage of time with blue corresponding to the beginning of the trajectory and red corresponding to the end. A mixed population of marine copepods *Acartia tonsa*, *Temora longicornis*, and *Eurytemora affinis* were used.

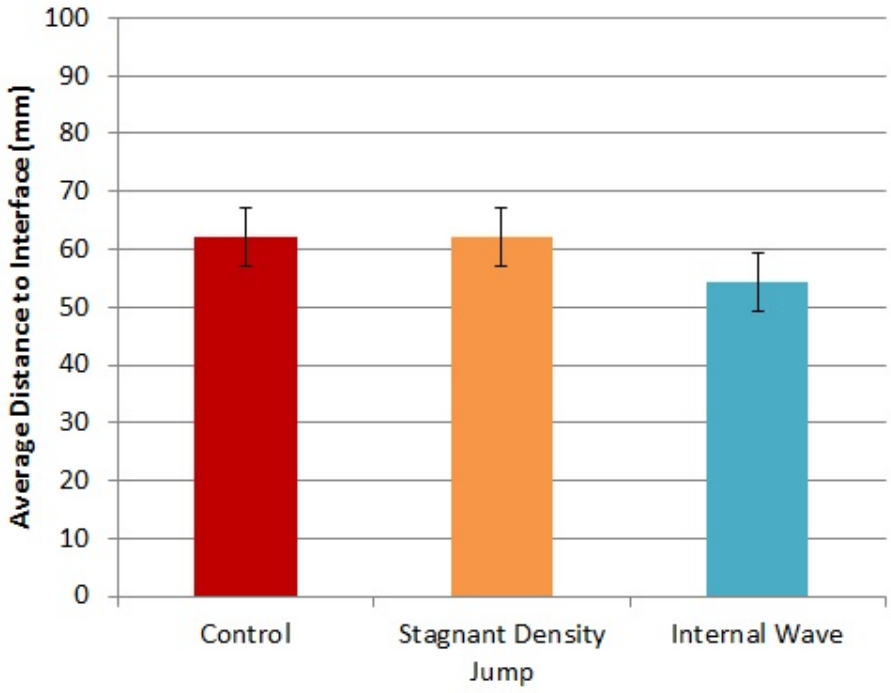

Figure 5.17: Time-averaged values of the absolute value of the vertical distance between the animal position and the interface location for the three treatments of the copepod behavior assays. 25 trajectories are included for each treatment.

To better understand the copepods' swimming behavior, the average of the absolute value of the vertical distance between the copepod position and the dynamic interface location was calculated. Figure 5.17 shows the values for each treatment. The control treatment yielded an average distance of 62.08 *mm*, the stagnant density jump treatment yielded 62.09 *mm*, and the internal wave treatment yielded 54.26 *mm*. The standard error for the three treatments were calculated to be 5.03. These results suggest that the copepods were preferentially located closer to the dynamic interface location in the standing internal wave treatment compared to the control and the stagnant density jump treatments either due to behavioral or physical forcing effects.

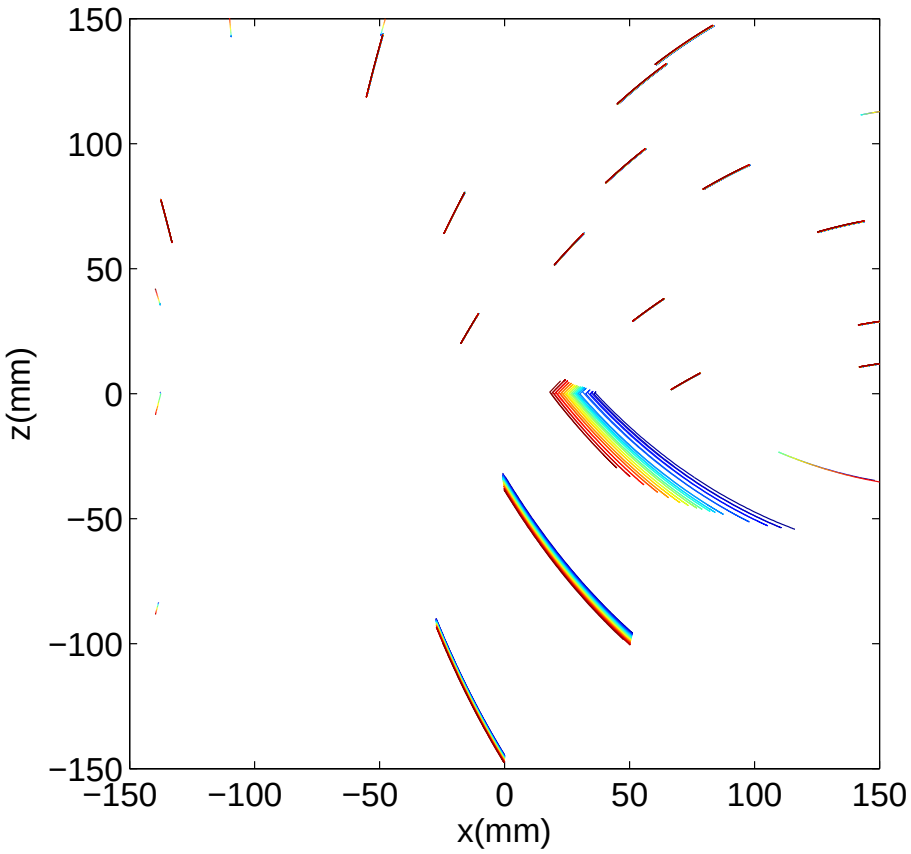

Figure 5.18: Theoretical trajectories of passive neutrally-buoyant particles in the same flow conditions as the internal wave treatment. Color indicates the passage of time with blue corresponding to the beginning of the trajectory and red corresponding to the end.

Trajectory analysis for neutrally-buoyant particles was performed to provide insight into whether the copepod trajectories observed in Figure 5.16 resulted from pure advection by the surrounding flow or whether animal behavior was a substantial contributor to the trajectory patterns. Figure 5.18 shows the neutrally-buoyant particle trajectories for the Case 2 internal wave conditions (i.e., matching the behavior trial flow conditions). The starting position for each trajectory was synced in time (frame

number) and position relative to an actual copepod trajectory observed in the behavior assays. The results show that the passive particles generally move in repetitive oscillations along invariant inclined paths. These passive particle trajectory shapes are enormously different in character compared to the loopy, orbital trajectories exhibited by copepods in the vicinity of the internal wave interface (Figure 5.16), which suggests animal behavior was a major contributor to the observed copepod motion.

As reported previously, the shear strain rate threshold level to evoke an escape response vary among copepod species ranging from $0.4-26\ s^{-1}$ (Yen and Fields 1992; Fields and Yen 1997a; Fields and Yen 1997b; Kiørboe et al. 1999; summarized in Woodson et al. 2014). For response of *A. tonsa* and *T. longicornis* to environmental flow structure (i.e., thin layer flow) the threshold for response was much smaller, around $0.025\ s^{-1}$ (Woodson et al. 2005). The response in this case consisted of excited area-restricted search behavior as part of a cue hierarchy in the search for food. For the current internal wave treatment, copepods experience a shear strain rate field that has peak values in a similar range to the threshold reported by Woodson et al. [2005]. Specifically, the theoretically calculated maximum shear strain rate value was around $0.044\ s^{-1}$ (Figure 5.9). The internal wave treatment also was different from the thin layer treatment because the flow is dynamic and time varying including periods in which the shear strain rate is below the threshold reported by Woodson et al. [2005] (see Figure 5.7). Nevertheless, the results here suggest a substantial animal behavior contribution to the trajectory shape and the shear strain rate values are consistent with the previously reported threshold to evoke excited area-restricted search behavior.

CHAPTER VI

SUMMARY AND CONCLUSIONS

6.1 Summary

A laboratory scale internal wave apparatus was used to create a standing internal wave for various physical arrangements that mimic conditions observed in the field. This experimental design was motivated by the objective to understand the bio-physical forcing in zooplankton transport in and near internal waves, where high levels of zooplankton densities have been observed.

A theoretical analysis of a standing internal wave inside a two-layer stratification system was conducted to derive the expressions for the independent variables controlling the wave motion. A boundary layer problem was setup assuming incompressible and irrotational flow. A series of boundary conditions, including bottom, kinetic, and dynamic conditions at the interface between the two layers and the free surface, was applied. Scaling analysis was used to justify a small-amplitude assumption, which linearized the equations. The analysis yielded expressions for the interface locations (η) and velocity potentials (ϕ) in terms of wave amplitude, wave number, seiching mode, and wave period. An expression for the velocity vector at each point in the domain was calculated by using the velocity potential function.

Three internal wave cases were targeted in the apparatus that correspond to density jumps of 0.75, 1.0, and 1.5 σ_t. Results from the flow characterizations for the three cases showed that when the density jump was greater than 1.0 σ_t (Cases 2 and 3), a standing internal wave was generated with a clean interface without any non-linear waves or mixing across the pycnocline. Signal processing of the interface location revealed that the generated frequency matched the target frequency. However, for

Case 1 with a density jump of 0.75 σ_t, inconsistent wave heights were observed. A broad range of peak frequencies, corresponding to 3 possible modes, was observed in the power spectral density. The undesirable characteristics were driven from forcing a harmonic mode that was too high. The mode number was increased to keep the wave period small (in order to avoid dissipation of the wave at very long periods). This forces the dominant frequency of oscillation to be higher, which increases the chance of non-linear waves being generated. Unfortunately, even with repeated trials, we were unsuccessful in creating a perfect standing internal wave for Case 1.

The zooplankton behavioral assays with a mixed population of marine copepods *Acartia tonsa*, *Temora longicornis*, and *Eurytemora affinis* were conducted in control (stagnant homogeneous fluid), stagnant density jump interface, and internal wave flow configurations. The results from tracking their swimming behavior revealed that the animals reacted to the density jump interface by showing a preferential horizontal motion parallel to the jump in the stagnant density jump environment. In the internal wave treatment, the copepods showed an acrobatic, orbital-like motion in and around the internal wave region (bounded by the crests and the troughs of the waves). In addition, the average distance of copepods to the density interface was less in the internal wave treatment compared to the control and stagnant pycnocline treatments. This suggests that copepods were preferentially located closer to the interface in the internal wave treatment, either due to physical transport or behavioral responses to the generated hydrodynamic cues. Theoretical trajectories of passive, neutrally-buoyant particles in the internal wave flow showed that they generally oscillated back-and-forth along fixed paths. This passive advection motion greatly contrasted the trajectories of the copepods motion, which were characterized as looping, orbital shapes in the region near the internal wave interface.

6.2 Conclusions

The flow characterization data collected through flow visualization, interface detection, and signal processing clearly indicated that our laboratory-scale internal wave apparatus was successful in mimicking the target wave parameters of amplitude, wave period, and the seiching mode. The 1.0 and 1.5 σ_t density-jump cases, in particular, were successful in generating a standing internal wave with wave properties that resembled *in situ* conditions. Furthermore, the density jump thresholds at which copepods (*A. tonsa* and *T. longicornis*) showed reluctance to cross the layers (Woodson et al. 2007a) ranged between 1.4 and 2.0 σ_t, which is in a similar and slightly greater range than the successful internal wave cases here. Therefore, it is reasonable to conclude that the internal wave apparatus is an effective and appropriate device for generating a standing internal wave at a pycnocline.

Furthermore, the internal wave apparatus is an appropriate platform for conducting copepod behavioral assays in an environment that mimics internal wave characteristics. Digital trajectories of the copepod in different physical arrangements revealed that a mixed-population of marine copepods preferred to swim near the interface and in the region bounded by the internal wave motion. A combination of the copepods affinity to swim closer to the interface and the repetitive motion of the neutrally-buoyant particles allows us to conclude that the copepods are not simply being advected by the flow. Instead, the copepods react to the dynamic motion of the internal waves by swimming in orbital trajectories.

6.3 Future Directions

The difficulties (i.e., variation in wave height and broad peak of the dominant oscillation frequency) in perfecting the 0.75 σ_t density-jump case for better range of density gradient studies can be address in future work. To resolve these issues, one could explore the option of decreasing the amplitude of the piston motion. Shortening

the tank length has the effect of decreasing the wavelength, thereby allowing a lower harmonic mode to be targeted. A potential negative effect is that the observation region for the behavioral assays would necessarily be much closer to the piston. Decreasing the amplitude of the piston motion potentially ensures the applicability of the small-amplitude assumption, which linearizes the waves, and thus potentially avoids the generation of non-linear waves. Both of these strategies require modification of the apparatus, but they should be relatively straightforward to implement.

The maximum velocity generated in our behavior assay was $\sim$16 $mm\ s^{-1}$ which was larger than the *in situ* parameters observed from field experiments, which was in the range of $1 - 12\ mm\ s^{-1}$ (Rinke et al. 2007; Vázquez et al. 2008). Using the theoretically-derived velocity expressions (Equations 3.44 - 3.47), one can see that the velocity magnitude can be lowered by decreasing the amplitude, and/or decreasing the wavenumber. These parameters are dictated in the internal wave apparatus, and they can be altered to meet the range of desired velocities with the caveat that a minimum amount of energy (input by the piston motion) is required to create stable internal wave flow.

Lastly, the preliminary copepod trials reported here are insightful and highlight the fact that copepod behavior plays a critical role around internal waves. Due to time and logistical constraints, a mixed-population of copepods was used here, but examining each species separately would provide new insight into their unique behaviors. Given the differences in swimming style, differences in architecture of their mechano-sensitive setal arrays, and differences in previously-reported responses to stagnant density-jump interfaces, it is reasonable to expect species-specific behavior. Thus, a more in-depth examination into how individual species of copepod respond to a range of internal wave characteristics is of interest.

References

A.L. Alldredge, T.J. Cowles, S. MacIntyre, J.E.B. Rines, P.L. Donaghay, C.F. Greenlaw, D.V. Holliday, M.M. Dekshenieks, J.M. Sullivan, and J.R.V. Zaneveld. Occurrence and mechanisms of formation of a dramatic thin layer of marine snow in a shallow Pacific fjord. *Marine Ecology Progress Series*, 233:1–12, 2002.

P.G. Baines. *Topographic effects in stratified fluids*. Cambridge University Press, Cambridge, 1995.

D.A. Birch, W.R. Young, and P.J.S. Franks. Thin layers of plankton: Formation by shear and death by diffusion. *Deep-Sea Research Part I*, 55:277–295, 2008.

P.K. Bjornsen and T.K. Nielsen. Decimeter scale heterogeneity in the plankton during a pycnocline bloom of *Gyrodinium aureolum*. *Marine Ecology Progress Series*, 73: 263–267, 1991.

L. Boegman and G.N. Ivey. Flow separation and resuspension beneath shoaling nonlinear internal waves. *Journal of Geophysical Research*, 114:C02018, 2009.

C. Bronmark and L. Hansson. *The Biology of Lakes and Ponds*. Oxford University Press, New York, 2005.

O.M. Cheriton, M.A. McManus, M.T. Stacey, and J.V. Steinbuck. Physical and biological controls on the maintenance and dissipation of a thin phytoplankton layer. *Marine Ecology Progress Series*, 378:55–69, 2009.

T.J. Cowles. Planktonic layers: Physical and biological interactions on the small scale. *In: Seuront L, Strutton PG (eds) Handbook of Scaling Methods in Aquatic Ecology: Measurement, Analysis, Simulation*. CRC Press, Boca Raton, FL, 2004.

T.J. Cowles and R.A. Desiderio. Resolution of biological microstructure through in situ fluorescence emission spectra: An oceanographic application using optical fibers. *Oceanography*, 6:105–111, 1993.

T.J. Cowles, R.A. Desiderio, and S. Neuer. *In situ* characterization of phytoplankton from vertical profiles of fluorescence emission spectra. *Marine Biology*, 115:217–222, 1993.

T.J. Cowles, R.A. Desiderio, and M.E. Carr. Small-scale planktonic structure: Persistence and trophic consequences. *Oceanography*, 11:4–9, 1998.

R.G. Dean and R.A. Dalrymple. *Water Wave Mechanics for Engineers and Scientists*. World Scientific, Singapore, 1991.

M.M. Dekshenieks, P.L. Donaghay, J.M. Sullivan, J.E.B. Rines, T.R. Osborn, and M.S. Twardowski. Temporal and spatial occurrence of thin phytoplankton layers in relation to physical processes. *Marine Ecology Progress Series*, 223:61–71, 2001.

J.B. Derenbach, H. Astheimer, H.P. Hansen, and H. Leach. Vertical microscale distribution of phytoplankton in relation to the thermocline. *Marine Ecology Progress Series*, 1:187–193, 1979.

P.G. Drazin and W.H. Reid. *Hydrodynamic Stability*. Cambridge University Press, Cambridge, 1981.

W.M. Durham, J.O. Kessler, and R. Stocker. Disruption of vertical motility by shear triggers formation of thin phytoplankton layers. *Science*, 323:1067–1070, 2009.

D.M. Fields and J. Yen. The escape behavior of marine copepods in response to a quantifiable fluid mechanical disturbance. *Journal of Plankton Research*, 19:1289–1304, 1997a.

D.M. Fields and J. Yen. Implications of the feeding current structure of *Euchaeta rimana*, a carnivorous pelagic copepod, on the spatial orientation of their prey. *Journal of Plankton Research*, 19:79–95, 1997b.

H.B. Fischer, E.J. List, R.C.Y. Koh, J. Imberger, and N.H. Brooks. *Mixing in Inland and Coastal Waters*. Academic Press, San Diego, CA, 1979.

P.J.S. Franks. Sink or swim: Accumulation of biomass at fronts. *Marine Ecology Progress Series*, 82:1–12, 1992.

P.J.S. Franks. Thin layers of phytoplankton: A model of formation by near-inertial wave shear. *Deep-Sea Research Part I*, 42:75–91, 1995.

S.M. Gallager, H. Yamazaki, and C.S. David. Contributions of fine-scale vertical structure and swimming behavior to formation of plankton layers on Georges Bank. *Marine Ecology Progress Series*, 267:27–43, 2004.

P. Gentien, M. Luven, M. Lehaitre, and J.L. Duvent. *In-situ* depth profiling of particle sizes. *Deep-Sea Research*, 42:1297–1312, 1995.

A. Gill. *Atmosphere - Ocean Dynamics*. Academic Press, New York, 1982.

K.B. Gretchen, M. Grosell, and K.V. Brix. Toxicity of silver, zinc, copper, and nickel to the copepod *Acartia tonsa* exposed via a phytoplankton diet. *Environmental Science and Technology*, 40:20632068, 2006.

H. Van Haren. Internal wave-zooplankton interactions in the Alboran Sea (W-Mediterranean). *Plankton Research*, 36:1124–1134, 2014.

L.R. Haury, M.G. Briscoe, and M.H. Orr. Tidally generated internal wave packets in Massachusetts Bay. *Nature*, 278:312–317, 1979.

L.R. Haury, P.H. Wiebe, and M.H. Orr. Tidally generated high-frequency internal wave packets and their effects on plankton in Massachusetts Bay. *Marine Research*, 41:65–112, 1983.

T.L. Hedrick. Software techniques for two- and three-dimensional kinematic measurements of biological and biomimetic systems. *Bioinspiration and Biomimetics*, 3: 034001, 2008.

D.F. Hill and M.A. Foda. Subharmonic resonance of short internal standing waves by progressive surface waves. *Journal of Fluid Mechanics*, 321:217–224, 1996.

D.V. Holliday, P.L. Donaghay, C.F. Greenlaw, D.E. McGehee, M.M. McManus, J.M. Sullivan, and J.L. Miksis. Advances in defining fine- and micro-scale pattern in marine plankton. *Aquatic Living Resources*, 16:131–136, 2003.

D.A. Horn, J. Imberger, and G.N. Ivey. The degeneration of largescale interfacial gravity waves in lakes. *Journal of Fluid Mechanics*, 434:181–207, 2001.

D.A. Horn, J. Imberger, G.N. Ivey, and L.G. Redekopp. A weakly nonlinear model of long internal waves in closed basins. *Journal of Fluid Mechanics*, 467:269–287, 2002.

E.L. Hult, C.D. Troy, and J.R. Koseff. The breaking of interfacial waves at a submerged bathymetric ridge. *Journal of Fluid Mechanics*, 637:45–71, 2009.

E.L. Hult, C.D. Troy, and J.R. Koseff. Harmonic generation of interfacial waves at a submerged bathymetric ridge. *Journal of Geophysical Research*, 115:C2, 2010.

E.L. Hult, C.D. Troy, and J.R. Koseff. The mixing efficiency of interfacial waves breaking at a ridge: 1. overall mixing efficiency. *Journal of Geophysical Research*, 116:C02003, 2011a.

E.L. Hult, C.D. Troy, and J.R. Koseff. The mixing efficiency of interfacial waves breaking at a ridge: 2. local mixing processes. *Journal of Geophysical Research*, 116:C02004, 2011b.

A.G. Humes. How many copepods? *Hydrobiologia*, 292/293:1–7, 1994.

P.J. Johnson, P.L. Donaghay, E.B. Small, and J.M. Sieburth. Ultrastructure and ecology of *Perispira ovum* (ciliophora: Litostomatea): An aerobic planktonic ciliate that sequesters the chloroplasts, itochondria and paramylon of *Euglena proxima* in a micro-oxic habitat. *Journal of Eukaryot Microbiology*, 422:323–335, 1995.

S. Kaartvedt, T.A. Klevjer, and D.L. Aksnes. Internal wave-mediated shading causes frequent vertical migrations in fishes. *Marine Ecology Progress Series*, 452:1–10, 2012.

T. Kiørboe, E. Saiz, and A. Visser. Hydrodynamic signal perception in the copepod *Acartia tonsa*. *Marine Ecology Progress Series*, 179:97–111, 1999.

G.S. Kleppel. On the diets of calanoid copepods. *Marine Ecology Progress Series*, 99:183, 1993.

P.K. Kundu, I.M. Cohen, and D.R. Dowling. *Fluid Mechanics*. Elsevier Academic Press, Waltham, MA, 2011.

Z. Lai, C. Chen, R.C. Beardsley, B. Rothschild, and R. Tian. Impact of high-frequency nonlinear internal waves on plankton dynamics in Massachusetts Bay. *Marine Research*, 68:259–281, 2010.

C.E. Lennert-Cody and P.J.S. Franks. Plankton patchiness in high-frequency internal waves. *Marine Ecology Progress Series*, 186:59–66, 1999.

C.E. Lennert-Cody and P.J.S. Franks. Fluorescence patches in high-frequency internal waves. *Marine Ecology Progress Series*, 235:29–42, 2002.

K.H. Mann and J.R.N. Lazier. *Dynamics of Marine Ecosystems*. Blackwell Science, Malden, MA, 1996.

J. Mauchline. *The Biology of Calanoid Copepods*. Academic Press, San Diego, 1998.

J.L. McGrath, H.J.S. Fernando, and J.C.R. Hunt. Turbulence, waves and mixing at shear-free density interfaces. Part 2: laboratory experiments. *Journal of Fluid Mechanics*, 347:235–261, 1997.

M.A. McManus, A.L. Alldredge, A.H. Barnard, E. Boss, J.F. Case, T.J. Cowles, P.L. Donaghay, L.B. Eisner, D.J. Gifford, C.F. Greenlaw, C.M. Herren, D.V. Holliday, D. Johnson, S. MacIntyre, D.M. McGehee, T.R. Osborn, M.J. Perry, R.E. Pieper, J.E.B. Rines, D.C. Smith, J.M. Sullivan, M.K. Talbot, M.S. Twardowski, A. Weidemann, and J.R. Zaneveld. Characteristics, distribution and persistence of thin layers over a 48 hour period. *Marine Ecology Progress Series*, 261:1–19, 2003.

M.A. McManus, O.M. Cheriton, P.J. Drake, D.V. Holliday, C.D. Storlazzi, P.L. Donaghay, and C.F. Greenlaw. Effects of physical processes on structure and transport of thin zooplankton layers in the coastal ocean. *Marine Ecology Progress Series*, 301:199–215, 2005.

C.B. Miller. *Biological Oceanography*. Blackwell Publishing, 2004.

O.M. Phillips. *The Dynamics of the Upper Ocean*. Cambridge University Press, Cambridge, 1969.

K. Rinke, I. Hübner, T. Petzoldt, S. Rolinski, M. König-Rinke, J. Post, A. Lorke, and J. Benndorf. How internal waves influence the vertical distribution of zooplankton. *Freshwater Biology*, 52:137–144, 2007.

J.P. Ryan, M.A. McManus, J.D. Paduan, and F.P. Chavez. Phytoplankton thin layers caused by shear in frontal zones of a coastal upwelling system. *Marine Ecology Progress Series*, 354:21–34, 2008.

W. Schmidt. *Sber. Akad. Wiss. Wien, Math. Nat. Class.*, 117:ABTH 2A, 1908.

M.T. Stacey, M.A. McManus, and J.V. Steinbuck. Covergences and divergences and thin layer formation and maintenance. *Limnology and Oceanography*, 52:1523–1532, 2007.

C.L. Stevens, P.J.H. Sutton, and C.S. Law. Internal waves downstream of Norfolk Ridge, Western Pacific, and their biophysical implications. *Limnology and Oceanography*, 57:897–911, 2012.

J.M. Sullivan, M.A. McManus, O.M. Cheriton, K.J. Benoit-Bird, L. Goodman, Z. Wang, J. Ryan, M. Stacey, D.V. Holliday, C. Greenlaw, M.A. Moline, and M. McFarland. Layered organization in the coastal ocean: An introduction to planktonic thin layers and the LOCO project. *Continental Shelf Research*, 30:1–6, 2010.

I.A. Svendsen. *Introduction to Nearshore Hydrodynamics*. World Scientific, Singapore, 2006.

S.A. Thorpe. On the shape of progressive internal waves. *Philosophical Transactions of the Royal Society of London. Series A, Mathematical and Physical Sciences*, 263: 563–614, 1968a.

S.A. Thorpe. On standing internal gravity waves of finite amplitude. *Journal of Fluid Mechanics*, 32:489–528, 1968b.

S.A. Thorpe. On the breaking of internal waves in the ocean. *Journal of Physical Oceanography*, 29:2433–2441, 1999.

J. Titelman. Swimming and escape behavior of copepod nauplii: Implications for predator-prey interactions among copepods. *Marine Ecology Progress Series*, 213: 203–213, 2001.

J. Titelman and T. Kiørboe. Motility of copepod nauplii and implications for food encounter. *Marine Ecology Progress Series*, 247:123–135, 2003a.

J. Titelman and T. Kiørboe. Predator avoidance by nauplii. *Marine Ecology Progress Series*, 247:137–149, 2003b.

C.D. Troy and J.R. Koseff. The instability and breaking of long internal waves. *Journal of Fluid Mechanics*, 543:107–136, 2005.

A.C. True. *Ecological Engines: Finescale Hydrodynamic and Chemical Cues, Zooplankton Behaviors, and Implications for Nearshore Marine Ecosystems*. PhD thesis, Georgia Institute of Technology, Atlanta, GA, 2014.

M. Umeyama. Experimental and theoretical analyses of internal waves of finite amplitude. *Journal of Waterway, Port, Coastal and Ocean Engineering*, 128:133–141, 2002.

A. Vázquez, M. Bruno, A. Izquierdo, D. Macías, and A. Ruiz-Cañavate. Meteorologically forced subinertial flows and internal wave generation at the main sill of the strait of gibraltar. *Deep-Sea Research I*, 55:1277–1283, 2008.

L. Velo-Suarez, L. Fernand, P. Gentien, and B. Reguera. Hydrodynamic conditions associated with the formation, maintenance and dissipation of a phytoplankton thin layer in a coastal upwelling system. *Continental Shelf Research*, 30:193–202, 2010.

E.A. Widder. Bioluminescence (US Navy's research). *Sea Technology*, 38:33–39, 1997.

P.H. Wiebe, C.S. Davis, and C.H. Greene. Visualizing life in the ocean interior. *Oceanus*, 35:100–106, 1992.

C.B. Woodson. *Thin Layers: Physical and Chemical Cues Contributing to Observed Copepod Aggregations*. PhD thesis, Georgia Institute of Technology, Atlanta, GA, 2005.

C.B. Woodson, D.R. Webster, M.J. Weissburg, and J. Yen. Response of copepods to physical gradients associated with structure in the ocean. *Limnology and Oceanography*, 50:1552–1564, 2005.

C.B. Woodson, D.R. Webster, M.J. Weissburg, and J. Yen. Cue hierarchy and foraging in calanoid copepods: ecological implications of oceanographic structure. *Marine Ecology Progress Series*, 330:163–177, 2007a.

C.B. Woodson, D.R. Webster, M.J. Weissburg, and J. Yen. The prevalence and implications of copepod behavioral responses to oceanographic gradients and biological patchiness. *Integrative and Comparative Biology*, 47:831–846, 2007b.

C.B. Woodson, D.R. Webster, and A.C. True. Copepod behavior: Oceanographic cues, distributions, and trophic interactions. In L. Seuront, editor, *Copepods: Diversity, Habitat, and Behavior*. Nova Publishers, 2014.

J. Yen and D.M. Fields. Escape responses of *Acartia hudsonica* (copepoda) nauplii from the flow field of *Temora longicornis* (copepoda). *Arch. Hydrobiol. Beih.*, 36: 123–134, 1992.